

Evaluating models for lithospheric loss and intraplate volcanism beneath the Central Appalachian Mountains

Maureen D. Long¹, Lara Suzanne Wagner², Scott D. King³, Rob L. Evans⁴, Sarah E Mazza⁵, Joseph Stephen Byrnes⁶, Elizabeth Johnson⁷, Eric Kirby⁸, Maximiliano Bezada⁶, Esteban Gazel⁹, Scott R. Miller¹⁰, John C. Aragon¹, and Shangxin Liu³

¹Yale University

²Carnegie Institution for Science

³Virginia Tech

⁴Woods Hole Oceanographic Institution

⁵Westfälische Wilhelms-Universität Münster

⁶University of Minnesota

⁷James Madison University

⁸University of North Carolina, Chapel Hill

⁹Department of Earth and Atmospheric Sciences, Cornell University

¹⁰University of Utah

November 21, 2022

Abstract

The eastern margin of North America has been shaped by a series of tectonic events including the Paleozoic Appalachian Orogeny and the breakup of Pangea during the Mesozoic. For the past ~200 Ma, eastern North America has been a passive continental margin; however, there is evidence in the Central Appalachian Mountains for post-rifting modification of lithospheric structure. This evidence includes two co-located pulses of magmatism that post-date the rifting event (at 152 Ma and 47 Ma) along with low seismic velocities, high seismic attenuation, and high electrical conductivity in the upper mantle. Here, we synthesize and evaluate constraints on the lithospheric evolution of the Central Appalachian Mountains. These include tomographic imaging of seismic velocities, seismic and electrical conductivity imaging along the MAGIC array, gravity and heat flow measurements, geochemical and petrological examination of Jurassic and Eocene magmatic rocks, and estimates of erosion rates from geomorphological data. We discuss and evaluate a set of possible mechanisms for lithospheric loss and intraplate volcanism beneath the region. Taken together, recent observations provide compelling evidence for lithospheric loss beneath the Central Appalachians; while they cannot uniquely identify the processes associated with this loss, they narrow the range of plausible models, with important implications for our understanding of intraplate volcanism and the evolution of continental lithosphere. Our preferred models invoke a combination of (perhaps episodic) lithospheric loss via Rayleigh-Taylor instabilities and subsequent small-scale mantle flow in combination with shear-driven upwelling that maintains the region of thin lithosphere and causes partial melting in the asthenosphere.

2
3
4
5
6 **Evaluating models for lithospheric loss and intraplate volcanism beneath the Central**
7 **Appalachian Mountains**
8
9

10 Maureen D. Long^{1*}, Lara S. Wagner², Scott D. King³, Rob L. Evans⁴, Sarah E. Mazza⁵, Joseph
11 S. Byrnes^{6,7}, Elizabeth A. Johnson⁸, Eric Kirby⁹, Maximiliano J. Bezada⁶, Esteban Gazel¹⁰, Scott
12 R. Miller¹¹, John C. Aragon^{1,12}, Shangxin Liu³
13
14

15 ¹Dept. Earth & Planetary Sciences, Yale University, New Haven, CT, USA

16 ²Earth & Planets Laboratory, Carnegie Institution for Science, Washington, DC, USA

17 ³Dept. Geosciences, Virginia Tech, Blacksburg, VA, USA

18 ⁴Dept. Geology & Geophysics, WHOI, Woods Hole, MA, USA

19 ⁵Dept. Geosciences, Smith College, Northampton, MA, USA

20 ⁶Dept. Earth & Environmental Sciences, University of Minnesota, Minneapolis, MN, USA

21 ⁷School of Earth & Sustainability, Northern Arizona University, Flagstaff, AZ, USA

22 ⁸Dept. Geology & Environmental Science, James Madison University, Harrisonburg, VA, USA

23 ⁹Dept. Geological Sciences, University of North Carolina at Chapel Hill, Chapel Hill, NC, USA

24 ¹⁰Dept. Earth & Atmospheric Sciences, Cornell University, Ithaca, NY, USA

25 ¹¹Dept. Geology & Geophysics, University of Utah, Salt Lake City, UT, USA

26 ¹²Now at: Earthquake Science Center, U.S. Geological Survey, Menlo Park, CA, USA

27 *Corresponding author. Email: maureen.long@yale.edu
28
29
30

31 *Submitted to Journal of Geophysical Research, 6/7/21*
32
33
34
35
36
37
38
39
40
41
42

43 **Key Points**

- 44 • There is a present-day geophysical anomaly in the upper mantle co-located with unusually
45 young volcanism in the Central Appalachians.
- 46 • We synthesize constraints from geophysics, petrology/geochemistry, and geomorphology
47 to constrain possible models for lithospheric loss.
- 48 • We favor one or more Rayleigh-Taylor lithospheric instabilities, perhaps in combination
49 with shear-driven upwelling.

50

51 **Abstract**

52 The eastern margin of North America has been shaped by a series of tectonic events
53 including the Paleozoic Appalachian Orogeny and the breakup of Pangea during the Mesozoic.
54 For the past ~200 Ma, eastern North America has been a passive continental margin; however,
55 there is evidence in the Central Appalachian Mountains for post-rifting modification of
56 lithospheric structure. This evidence includes two co-located pulses of magmatism that post-date
57 the rifting event (at 152 Ma and 47 Ma) along with low seismic velocities, high seismic attenuation,
58 and high electrical conductivity in the upper mantle. Here, we synthesize and evaluate constraints
59 on the lithospheric evolution of the Central Appalachian Mountains. These include tomographic
60 imaging of seismic velocities, seismic and electrical conductivity imaging along the MAGIC array,
61 gravity and heat flow measurements, geochemical and petrological examination of Jurassic and
62 Eocene magmatic rocks, and estimates of erosion rates from geomorphological data. We discuss
63 and evaluate a set of possible mechanisms for lithospheric loss and intraplate volcanism beneath
64 the region. Taken together, recent observations provide compelling evidence for lithospheric loss
65 beneath the Central Appalachians; while they cannot uniquely identify the processes associated

66 with this loss, they narrow the range of plausible models, with important implications for our
67 understanding of intraplate volcanism and the evolution of continental lithosphere. Our preferred
68 models invoke a combination of (perhaps episodic) lithospheric loss via Rayleigh-Taylor
69 instabilities and subsequent small-scale mantle flow in combination with shear-driven upwelling
70 that maintains the region of thin lithosphere and causes partial melting in the asthenosphere.

71

72 **Plain Language Summary**

73 For the past 200 million years, the east coast of North America has been situated in the
74 middle of a tectonic plate. Contrary to the expectations for this setting, a region of the Central
75 Appalachian Mountains centered near the boundary between the U.S. states of Virginia and West
76 Virginia exhibits atypical properties. The unusual observations include volcanic activity in the
77 geologic past far away from a plate boundary, elevated rates of erosion associated with high
78 topography in the Central Appalachians, and anomalous structure in the upper mantle that has been
79 detected using geophysical methods. This paper describes, synthesizes, and compares a suite of
80 observations that show that this part of the Central Appalachians is unusual compared to other so-
81 called passive continental margins. We discuss a range of different models that might describe
82 how the lithosphere, or the rigid part of the crust and upper mantle that defines the tectonic plate,
83 has evolved through time beneath our study region. We show that the lithosphere today is thin,
84 and that past episodes of lithospheric loss involving a portion of dense lithosphere “dripping” into
85 the mantle under the force of gravity may provide a good explanation for the observations.

86

87

88

89 **1. Introduction**

90 Perhaps one of the most surprising and perplexing observations made over the past fifteen
91 years of EarthScope and related science is the presence of an apparent “hole” in the lithosphere
92 beneath the central Appalachians in Virginia and West Virginia that correlates very closely with
93 the presence of comparatively recent (Late Jurassic and Eocene) volcanism. While the eastern
94 margin of North America has undergone a series of major tectonic events over the past billion
95 years of Earth history, these events significantly pre-date the volcanic episodes. The Grenville
96 orogeny that took place at roughly 1 Ga culminated in the formation of the supercontinent Rodinia
97 (e.g., McLelland et al., 2010; Whitmeyer & Karlstrom, 2007); Rodinia subsequently broke up
98 between 750 and 550 Ma (e.g., Burton & Southworth, 2010; Li et al., 2008). The subsequent
99 Appalachian orogenic cycle encompassed a protracted series of terrane accretion and mountain
100 building events during the Paleozoic (e.g., Hatcher, 2010; Hibbard et al., 2010). The Pangea
101 supercontinent was formed during the last phase of the Appalachian orogeny as Laurentia was
102 joined to Gondwana. The breakup of Pangea, the final major tectonic event to affect the central
103 Appalachians, began at roughly 230 Ma with rifting and extension, and the rift-to-drift transition
104 was complete by approximately 185 Ma (e.g., Withjack et al., 1998; 2012). Rifting was
105 accompanied by the emplacement of the Central Atlantic Magmatic Province (CAMP), one of the
106 Earth’s largest igneous provinces, over a period of less than one million years at approximately
107 200 Ma (e.g., Blackburn et al., 2013; Marzoli et al., 2018; McHone, 1996). Eastern North America
108 thus assumed its current status as a passive continental margin by ~185 Ma, some 35 Ma before
109 the first episode of anomalous central Appalachian volcanism.

110 The central Appalachians are not the only region to present evidence for passive margin
111 lithospheric evolution. Across eastern North America, there are hints that, in some places,

112 modifications to lithospheric structure after the last major tectonic event (the breakup of Pangea
113 and the opening of the Atlantic Ocean basin) may have been profound. For example, there is
114 evidence for alkaline volcanism that post-dates CAMP in several regions along the margin (e.g.,
115 Mazza et al., 2017), including Jurassic kimberlitic magmatism in New York and Pennsylvania
116 (e.g., Bailey & Lupulescu, 2015; Bikerman et al., 1997), the Jurassic White Mountain Magma
117 Series and younger Cretaceous magmatism in New England (e.g., Foland et al., 1971; Kinney et
118 al., 2019), and the Cretaceous Monteregeian Hills in eastern Canada (e.g., Foland et al., 1986).
119 Recent seismic imaging of upper mantle structure beneath eastern North America using data from
120 the EarthScope USArray Transportable Array (TA) has revealed evidence for complex upper
121 mantle structure (e.g., Biryol et al., 2016; Golos et al., 2018; Liu & Holt, 2015; Porter et al., 2016;
122 Schmandt & Lin, 2014; Wagner et al., 2018), including several prominent low velocity anomalies
123 that may hint at recent or ongoing dynamic processes. Furthermore, there is evidence from
124 geomorphological investigations for relatively recent rejuvenation of Appalachian topography
125 (e.g., Gallen et al., 2013; Miller et al., 2013; Pazzaglia & Brandon, 1996), perhaps reflecting
126 changes in dynamic topography generated by deep mantle flow (e.g., Rowley et al., 2013;
127 Spasojevic et al., 2008) and/or temporal changes in the density structure of the crust or mantle
128 lithosphere (e.g., Fischer, 2002; Wagner et al., 2012). Finally, there is ample seismicity along the
129 eastern North American margin (e.g., Wolin et al., 2013), much of it concentrated in zones that
130 may represent the reactivation of ancient structures in the present-day stress field (e.g., Thomas &
131 Powell, 2017).

132 Here we focus on the Central Appalachian Mountains, in a region encompassing the
133 boundary between Virginia and West Virginia (Figure 1). This region has hosted two pulses of
134 (spatially co-located) post-CAMP volcanism (at 152 Ma and 47 Ma; Mazza et al., 2014; 2017),

135 with the latter representing the youngest magmatic event in eastern North America. Taking
136 advantage of newly available data from EarthScope and related projects, recent geophysical
137 imaging has yielded evidence for anomalous structures in the crust and upper mantle beneath this
138 region. This includes a prominent zone of low seismic velocities (e.g., Schmandt & Lin, 2014;
139 Wagner et al., 2018), high seismic attenuation (Byrnes et al., 2019), and high electrical
140 conductivity (Evans et al., 2019) in the upper mantle, with further evidence for thin mantle
141 lithosphere from receiver function analysis (Evans et al., 2019). The seismic structure beneath the
142 region is anomalous in several other ways, including a sharp lateral transition in crustal thickness
143 (along a profile that is perpendicular to the strike of the Appalachian Mountains; Long et al., 2019)
144 and an abrupt transition in SKS splitting behavior (Aragon et al., 2017).

145 The goal of this paper is to synthesize a suite of recent results from the Central Appalachian
146 Mountains that have been enabled by EarthScope, GeoPRISMS, and related efforts in eastern
147 North America. These include seismic and magnetotelluric imaging of the subsurface using data
148 from the USArray Transportable and Flexible Arrays, geochemical and petrological investigations
149 of post-CAMP magmatic products, geomorphological investigations of present-day erosion rates,
150 and analysis of gravity and heat flow data. We include results from the MAGIC (Mid-Atlantic
151 Geophysical Integrative Collaboration) experiment, which deployed a suite of densely spaced, co-
152 located broadband seismic and magnetotelluric observatories across the Central Appalachians
153 (Long et al., 2020). We discuss possible mechanisms for lithospheric loss and intraplate volcanism
154 beneath the Central Appalachians and for the persistence of anomalous lithospheric structure over
155 geologic time. These possible mechanisms include catastrophic lithospheric loss via Rayleigh-
156 Taylor instability, gradual thermal erosion of the lithosphere, edge-driven convection, a deep
157 mantle source of heat and/or hydration, shear-driven upwelling, or a combination of these. We

158 evaluate the strengths and weaknesses of different models and discuss how well each explains the
159 full range of observations. We present our preferred scenarios for lithospheric loss and intraplate
160 volcanism beneath the Central Appalachians, which invoke a combination of Rayleigh-Taylor
161 instability and shear-driven upwelling and/or small-scale mantle flow. Finally, we explore the
162 implications for a range of important outstanding Earth science questions and suggest avenues for
163 future progress on understanding the evolution of the Central Appalachians in particular and
164 continental lithosphere in general.

165

166 **2. Geophysical constraints**

167 *2.1 Seismic observations*

168 *2.1.1 Tomographic imaging of the Central Appalachian Anomaly*

169 Since the EarthScope TA traversed the eastern United States, a significant number of
170 papers have been published that image a volume of upper mantle with low seismic velocities that
171 has come to be known as the Central Appalachian Anomaly (CAA; e.g., Schmandt & Lin, 2014).
172 Data for these studies include Rayleigh waves from both ambient noise cross correlations (Bensen
173 et al., 2008; Golos et al., 2018; Pollitz & Mooney, 2016; Porter et al., 2016; Savage et al., 2017;
174 Schmandt & Lin, 2014; Schmandt et al., 2015; Shen & Ritzwoller, 2016; Wagner et al., 2018; Xie
175 et al., 2018) and teleseismic earthquakes (Babikoff & Dalton, 2019; Golos et al., 2018; Pollitz &
176 Mooney, 2016; Porter et al., 2016; Schaeffer & Lebedev, 2014; Schmandt et al., 2015; Shen &
177 Ritzwoller, 2016; Wagner et al., 2018; Yuan et al., 2014). Some studies have relied on teleseismic
178 body waves (Biryol et al., 2016; Golos et al., 2018; Savage, 2021; Schmandt & Lin, 2014; Wang
179 et al., 2019) and body waves from local seismicity (Wang et al., 2019).

180 The methodologies employed for determining spatial variations in velocity vary as well,
181 particularly for those studies determining Rayleigh wave phase velocity maps that are
182 subsequently inverted to create 3D shear wave velocity models. Several studies employed
183 gradiometry (Lin et al., 2009) and/or Helmholtz (Lin & Ritzwoller, 2011) or Helmholtz-like
184 (Pollitz & Snoke, 2010) wavefront modeling approaches that avoid the need for inversion and
185 associated regularization (Babikoff & Dalton, 2019; Pollitz & Mooney, 2016; Porter et al., 2016;
186 Schmandt et al., 2015; Shen & Ritzwoller, 2016) but that do depend on the grid spacing for the
187 calculated derivatives (Babikoff & Dalton, 2019). Of those studies that used inverse approaches,
188 either for determining phase velocity maps or for body wave imaging, most used sensitivity kernels
189 that incorporate finite frequency effects (Biryol et al., 2016; Golos et al., 2018; Savage et al., 2017;
190 Schmandt & Lin, 2014; Wagner et al., 2018). Additionally, some studies used full waveform
191 inversions of fundamental mode Rayleigh waves (Schaeffer & Lebedev, 2014; Yuan et al., 2014).

192 Despite the diversity of imaging approaches, most of these studies presented strikingly
193 similar results in their identification of a small region of decreased seismic velocities in the
194 uppermost mantle near the central WV/VA border. Figure 2 shows horizontal slices through the
195 uppermost mantle (depth = 80 – 100 km) for a selection of six models that cover the CAA region
196 (Boyce et al., 2019; Porter et al., 2016; Schmandt & Lin, 2014; Schmandt et al., 2015; Shen &
197 Ritzwoller, 2016; Wagner et al., 2018). Three of these used a gradiometry/Helmholtz tomographic
198 approach (Porter et al., 2016; Schmandt et al., 2015; Shen & Ritzwoller, 2016); Schmandt et al.
199 (2015) and Shen & Ritzwoller (2016) added additional constraints from receiver functions and/or
200 H/V ratios. Wagner et al. (2018) used a finite-frequency two-plane wave inversion for the
201 determination of their phase velocity maps (Yang & Forsyth, 2006). Schmandt & Lin (2014)
202 inverted teleseismic P and S-wave body waves with constraints from ambient noise phase

203 velocities to better define shallow structure. Boyce et al. (2019) performed an inversion of
204 teleseismic P-wave body waves without any input from surface waves. All of these models show
205 a very localized low-velocity region in the uppermost mantle, with lateral dimensions that are
206 comparable to the interstation spacing of the TA and/or to the grid-node spacing employed in the
207 inversion. This suggests that the anomaly may well be smaller than imaged, but it is unlikely to be
208 much larger.

209 The surface wave-based models (Porter et al., 2016; Schmandt et al., 2015; Shen &
210 Ritzwoller, 2016; Wagner et al., 2018) allow us to compare the absolute shear wave velocities
211 observed within the uppermost mantle. Figure 3 shows cross-sections through all four models
212 along transects roughly parallel to the MAGIC deployment. All of the seismic profiles show an
213 abrupt decrease in seismic velocities (4.4 - 4.5 km/sec) for a relatively small region (< 150 km)
214 along strike. This contrasts with the shear wave velocities observed at the same depth to the north
215 and west which generally exceed 4.6 km/sec, consistent with relatively cold continental mantle
216 lithosphere. Velocities also increase somewhat to the east of the CAA (between 4.5 - 4.6 km/sec),
217 though these velocities are notably not as fast as those observed to the north and west ($V_s > 4.6$).
218 Crustal velocities within the CAA are normal-to-slightly-elevated in the region above or near the
219 low velocities in the uppermost mantle. There is no evidence in any model of reduced crustal
220 seismic velocities associated with the CAA, as might be expected in the presence of a high
221 geothermal gradient.

222

223 *2.1.2 Seismic imaging across the dense MAGIC transect*

224 The MAGIC seismic experiment (Long et al., 2020), part of the USArray Flexible Array,
225 consisted of a linear deployment (roughly perpendicular to the strike of the Appalachian

226 Mountains) of 28 densely spaced broadband seismic stations across the CAA (Figure 1). The
227 nominal station spacing was ~15 km in the region with anomalous post-CAMP volcanism and just
228 under 30 km elsewhere. Estimates of depth to Moho across the MAGIC array derived from P-to-
229 S receiver functions (Long et al., 2019) reveal evidence for a sharp “step” in the Moho just to the
230 east of the Blue Ridge mountains (Figure 3; purple diamonds/line). This step involves a change in
231 crustal thickness from roughly 48 km to the west to ~ 35 km to the east over a distance of ~15 km
232 (Figure 3). The Moho step is located approximately 80 km to the east of the easternmost Eocene
233 volcanic formation (Mole Hill, outside Harrisonburg, VA; see Figure 1). The step in the Moho
234 does not appear to be a feature that is unique to the Central Appalachians; Li et al. (2020) argued
235 that there is a Moho step near the western edge of Laurentian terranes throughout much of the
236 central and northern Appalachians, extending north to roughly 43° latitude.

237 MAGIC data have also been used to document a sharp lateral transition in SKS splitting
238 behavior across the Central Appalachian Mountains (Aragon et al., 2017). Figures 2 & 3 show
239 SKS splitting measurements at stations of the MAGIC array; these exhibit a sharp transition from
240 NE-SW fast directions at stations in the Appalachian Mountains to more E-W fast directions at
241 stations located just to the east of the mountains. This transition in splitting behavior is roughly
242 co-located with the easternmost occurrences of the post-CAMP igneous formations in the region.
243 Aragon et al. (2017) suggested that SKS splitting reflects a combination of contributions from
244 present-day mantle flow in the asthenosphere and lithospheric anisotropy frozen in from past
245 tectonic processes. They further proposed that the lateral transition in splitting behavior is
246 controlled mainly by the lithospheric component, although we explore an alternative explanation
247 (one that invokes small-scale mantle flow) for this observation in this paper.

248 Constraints on present-day lithospheric thickness across the MAGIC array were obtained
249 by Evans et al. (2019) through S_p receiver function imaging of the lithosphere-asthenosphere
250 boundary (LAB). Their interpretations of the images suggest a lithospheric thickness of roughly
251 100-120 km beneath the eastern part of the MAGIC array. Directly beneath the Appalachian
252 Mountains, Evans et al. (2019) identified a converter at ~80-90 km depth that dips gently to the
253 west, likely corresponding to the LAB. Beneath the western half of the MAGIC array, a flat-lying
254 converter at a depth of ~90 km likely corresponds to a mid-lithospheric discontinuity (MLD), while
255 far to the west a prominent converter at a depth of ~140 km likely corresponds to the base of the
256 lithosphere. Importantly, the S_p receiver function analysis of Evans et al. (2019) suggested thin
257 (~80-90 km) lithosphere co-located with the tomographically imaged CAA.

258 Another result from the MAGIC experiment, based on seismic attenuation measurements,
259 also suggests thin lithosphere beneath the Appalachian Mountains. Byrnes et al. (2019) modeled
260 variations in the waveforms of first-arriving P phases from deep earthquakes recorded at MAGIC
261 seismic stations using the approach of Bezada (2017) and Bezada et al. (2019). The result is a map
262 of Δt^* values (Figure 2, grayscale; Figure 3, red line), a metric that is more positive when
263 attenuation is stronger. Byrnes et al. (2019) observed low Δt^* values at the eastern and western
264 ends of the MAGIC array, with much higher values (0.26 s) directly above the tomographically
265 imaged CAA (Figures 2 & 3). For context, a 50 to 150 km change in lithospheric thickness, with
266 V_p and Q_p values taken from the lithosphere and asthenosphere in PREM (Dziewonski and
267 Anderson, 1981), leads to Δt^* of only 0.03 to 0.09 s. Extrinsic attenuation due to either short- or
268 long-wavelength variations in seismic velocity cannot explain the maximum in Δt^* at the CAA
269 (Byrnes et al., 2019); rather, a thin lithosphere and particularly high attenuation in the
270 asthenospheric upper mantle are required by the observations. Byrnes et al. (2019) suggested that

271 the values of Q_p for the asthenospheric upper mantle beneath the CAA are low enough to require
272 either partial melt (e.g., Abers et al., 2014) or a premelting effect that involves the disordering of
273 grain boundaries as the solidus is approached (Yamauchi and Takei, 2016). More broadly, the
274 attenuation results exclude the presence of either thick lithosphere or the replacement of
275 lithosphere with “normal” sub-solidus asthenosphere in the CAA region.

276 MAGIC data were also used to investigate the detailed structure of the mantle transition
277 zone beneath the Central Appalachians (Liu et al., 2018). Because the phase transformations
278 associated with the 410 and 660 km mantle discontinuities are sensitive to temperature and water
279 content, a detailed characterization of the transition zone can shed light on the thermal and
280 hydration state of the mid-mantle and can reflect possible contributions from vertical mantle flow
281 or from the presence of lithospheric fragments sinking through the mid-mantle (e.g., Benoit et al.,
282 2013; Bina & Helffrich, 1994; Schmandt et al., 2012; Smyth & Frost, 2006). Images of the
283 transition zone beneath the MAGIC array derived from single-station stacking of P wave receiver
284 functions, migrated to depth using the iasp91 velocity model (Kennett and Engdahl, 1991), are
285 shown in Figure 4. These images reveal that both the 410 and the 660 km discontinuities seem to
286 deepen smoothly from west to east across the array, though the estimated thickness of the transition
287 zone (which should be relatively insensitive to 3D velocity variations, which are not accounted for
288 in our analysis) remains relatively constant. Previous work on transition zone structure beneath the
289 southeastern U.S. using permanent seismic stations (Long et al., 2010) similarly suggested that
290 transition zone thickness was generally uniform across the region and did not deviate significantly
291 from standard mantle models. Keifer and Dueker (2019) applied Ps receiver function analysis to
292 data throughout the central and eastern U.S. and found evidence for a region of anomalously thin
293 (~230 km, as opposed to a nominal thickness of 250 km) transition zone beneath our study region.

294 However, they also found evidence for transition zone thinning beneath much of the eastern U.S.,
295 so this feature was not specific to the Central Appalachians. Work by Gao and Liu (2014) found
296 little evidence for transition zone thinning beneath the eastern U.S. based on receiver functions;
297 Wang and Pavlis (2016), who applied a 3-D wavefield imaging method, similarly found evidence
298 for a generally standard transition zone thickness beneath our study region. The absence of
299 significant variability in transition zone thickness across the MAGIC array suggests that there is
300 likely little variation in the temperature or hydration state of the transition zone associated with
301 the CAA anomaly. An alternative possibility is that any effects of lateral variations in temperature
302 and hydration effectively balance each other out.

303

304 *2.2 Electrical conductivity observations*

305 Magnetotelluric data, collected as part of the MAGIC experiment (Long et al., 2020) and
306 augmented by EarthScope TA coverage, highlight significant variations in lithospheric thickness
307 across this portion of the central Appalachians (Evans et al., 2019). The electrical conductivity
308 model of Evans et al. (2019), shown in Figure 3 (panel E), yields evidence for a variety of features,
309 including thick lithosphere (>150 km) beneath the western part of the MAGIC profile and thin
310 lithosphere (<75 km) directly along the CAA. In between the thick lithosphere to the NW and the
311 thin lithosphere of the CAA lies a region of more conductive mantle at depths between ~100km-
312 180km (100 – 400 km distance along the profile). Evans et al. (2019) interpreted this area as
313 comprising lithospheric mantle affected by a combination of hydration and/or deformation
314 (Pommier et al., 2018) that occurred during Grenville orogenic suturing. The conductivities of the
315 CAA at depths greater than 80km are sufficiently high (> 0.1 S/m, corresponding to < 10 ohm-m)
316 to require the presence of a small volume of partial melt (Evans et al., 2019). The inferences on

317 lithospheric thickness beneath the Appalachians gleaned from the electrical conductivity model
318 are consistent with constraints from Sp receiver function analysis, and Evans et al. (2019)
319 interpreted these datasets jointly.

320

321 *2.3 Gravity and heat flow observations*

322 In Figure 5A we show a map of Bouguer gravity anomaly from PACES (e.g., Stein et al.,
323 2014) in a region surrounding the CAA. The well-known gravity low over the Appalachian
324 topographic high and gravity high over the Piedmont are apparent in the Bouguer gravity plot
325 (Pratt et al., 1988). The transition between the two is the Appalachian gravity gradient. Crustal
326 thickening beneath the Appalachian Mountains has been proposed to explain the gravity low
327 (Cook, 1984), while several explanations have been proposed for the gravity high. Interpretations
328 have noted the correlations between the gravity high and the Carolina Slate (Long, 1979) or
329 Mesozoic rift basins (Griscom, 1963), or attributed the gravity high to dipping structures imaged
330 in seismic reflection data (Hutchinson et al., 1986) or subsurface loading (Karner & Watts, 1983).
331 Following Stein et al. (2014), we upward continued the Bouguer anomaly data to 40 km and
332 subtracted the result from the original Bouguer anomaly data, creating a “reduced” or upward
333 continued Bouguer gravity map (Figure 5B). This procedure enhances anomalies from sources at
334 greater depth and suppresses those from near surface sources (Jacobsen, 1987). We observed no
335 striking correlation between the reduced Bouguer gravity map and the slow wavespeed anomaly
336 documented in tomographic models (Figures 2 and 3) associated with the CAA, suggesting that
337 there is no strong gravity anomaly associated with the other geophysical anomalies. The reduced
338 Bouguer gravity map (Figure 5B) does show some hint of a gravity low in the CAA region, with
339 a maximum amplitude of perhaps 35 mgal; however, there are similar gravity lows elsewhere along

340 strike in the central Appalachians, and there is no localized anomaly that matches the dimensions
341 of the tomographically imaged CAA.

342 It is reasonable to question whether we would in fact expect to see a gravity anomaly due
343 to a thermal anomaly in the uppermost mantle that has the dimensions of the tomographically
344 imaged CAA. To illustrate the expected impact of a slow seismic anomaly on gravity, we assume
345 that the anomaly is purely thermal. The temperature and density anomaly due to a thermal anomaly
346 will be related by the coefficient of thermal expansion,

$$347 \quad \delta\rho = -\rho\alpha\delta T \quad (1)$$

348 where ρ is the density, α is the coefficient of thermal expansion and T is the temperature, the minus
349 sign indicates that a higher temperature results in a decrease in density. Using the solution for the
350 gravity anomaly due to a buried sphere (Turcotte & Schubert, 2002) with a sphere of radius 50 km
351 centered at 100 km depth, matching the peak 35 mgal gravity anomaly associated with the CAA
352 requires a density contrast of -100 kg m^{-3} . This requires an unrealistically large temperature
353 contrast of 1000°C from Equation 1, with $\rho = 3300 \text{ kg/m}^3$ and $\alpha = 3.0 \times 10^{-5}^\circ\text{C}^{-1}$. A more
354 realistic temperature contrast of $100\text{-}200^\circ\text{C}$ produces a Bouguer gravity anomaly of $3.5\text{-}7 \text{ mgals}$,
355 which is small enough that it is unlikely to be observed. Using Birch's law (Birch, 1961),

$$356 \quad v_p = -1.87 + 0.00305\rho, \quad (2)$$

357 where v_p is p wave velocity in km s^{-1} and ρ is density in kg m^{-3} , a 3% anomaly in v_p produces a
358 3% change in ρ . Hence, a 3% change in ρ is equivalent to -100 kg m^{-3} , assuming an upper mantle
359 density of 3300 kg m^{-3} . While a direct comparison between a reasonable absolute v_p anomaly, as
360 constrained by gravity data, and tomographic models (which constrain either absolute v_s or
361 relative v_p values) is not straightforward, a 3% v_p anomaly is generally consistent with
362 tomographic constraints.

363 This simple calculation, and the fact that we image a slow velocity anomaly of several
364 percent beneath the CAA, but no large or prominent gravity anomaly that matches its dimensions,
365 suggests that the anomaly is unlikely to be purely thermal; much of the velocity reduction may be
366 due instead to the presence of partial melt and/or water. However, this inference would be
367 complicated if there is also material with excess (positive) density in the crust or mantle
368 lithosphere; in this case, the gravity signature from the less dense material (in the asthenospheric
369 upper mantle) would destructively interfere with that from the more-dense material.

370 Inferences on the thermal state of the crust and lithosphere can in principle be gleaned from
371 heat flow measurements and from the distribution of thermal springs in and around our study area;
372 however, these indicators are difficult to interpret. The Virginia-West Virginia Hot Springs region
373 (Bath and Highland Counties, Virginia and Pocahontas county, West Virginia, just to the south
374 and west of the central part of the CAA) has the largest concentration of thermal springs in the
375 eastern US, with more than 50 springs (Waring, 1965). Three prominent hot springs are shown in
376 Figure 5. With the exception of one anomalously high heat flow value that is thought to be
377 contaminated by groundwater circulation, heat flow in the Virginia-West Virginia Hot Springs
378 region is consistent with the regional trend (Perry et al., 1979; Frone et al., 2015). As discussed by
379 Evans et al. (2019), slightly elevated heat flow is observed across the Appalachians, with values
380 between 70-80 mW/m² across the mountains (Frone et al., 2015). Overall, then, the evidence for
381 locally high heat flow in the CAA region is mixed; while thermal springs are present, heat flow
382 data do not show a pronounced anomaly in the vicinity of the CAA.

383

384

385

386 **3. Petrological and geochemical constraints**

387 The Central Appalachians have experienced two pulses of magmatism following the rifting
388 of Pangea at 152 Ma and 47 Ma, co-located in a roughly 80 km by 50 km region that straddles the
389 Virginia-West Virginia border (Johnson et al., 1971; Southworth et al., 1993; Mazza et al., 2014;
390 2017; Figure 1). The Late Jurassic magmatic event is characterized by a bimodal population of
391 highly alkaline rocks, comprised of low silica basanites and high silica phonolites (Figure 6A).
392 Mazza et al. (2017) explained the bimodal population as a result of fractional crystallization of the
393 basanites at 10 kbar/35 km depth, near the base of an assumed 40 km thick crust. Calculated mafic
394 melt equilibration temperatures from the Late Jurassic volcanics are consistent with normal
395 asthenospheric mantle (~1350 °C, 2 GPa) and are too cold to invoke melting from a mantle plume
396 (Mazza et al., 2017), but these calculations are limited to only one sample containing olivine.
397 Radiogenic isotopes have been used as indicators for both assessing crustal interaction and
398 differentiating mantle reservoirs. While Mazza et al. (2017) showed that the Late Jurassic event
399 likely was unaffected by crustal assimilation, the geochemical and isotopic datasets for Central
400 Appalachian crustal basement rocks are limited and do not include any of the mid-upper crustal
401 carbonates that are abundant in the region. The Late Jurassic volcanics have a range of Pb
402 radiogenic isotopes similar to volatile-rich lithologies such as carbonatites and kimberlites, with
403 enrichment of radiogenic Pb coupled to magma evolution. Sr-Nd radiogenic isotopes are nearly
404 identical to values reported from Late Jurassic kimberlites in New York (Figure 6C; Bailey &
405 Lupulescu, 2015), which trend towards an enriched mantle component. The radiogenic isotope
406 signatures from the Late Jurassic magmatic event in the Central Appalachians have been
407 interpreted as melting of an enriched mantle source, mixing with an unsampled highly radiogenic
408 Pb source that is potentially associated with metasomatism that is typical of kimberlite/carbonatite

409 magmas. Trace element signatures (Figure 6B) also imply the Late Jurassic basanites were
410 produced from low degree melting of an enriched asthenospheric source (~70 km depth).

411 The Eocene magmatic event is also characterized by bimodal, alkaline rocks, but these are
412 silica-saturated and are also characterized by lower abundance of alkaline elements than the Late
413 Jurassic event. The mafic population is comprised of microbasalt to basalt magma containing Al-
414 augite and olivine phenocrysts, while the felsic population has an average trachydacite
415 composition (Figure 6A). Similar to the Late Jurassic event, the bimodal nature of the Eocene
416 event can be explained by fractional crystallization, with the felsic magmas forming at shallow
417 crustal depths of 2 kbar/7 km (Mazza et al., 2017). The Eocene mafic magmas are characterized
418 by typical ocean island basalt trace element signatures, suggesting they are the product of melting
419 an asthenospheric source (Figure 6B), in agreement with calculated mafic melt equilibration
420 temperatures and pressures consistent with normal asthenospheric mantle (~1400 °C and 2.3 GPa;
421 Mazza et al., 2014). The Eocene magmatic event was not affected by crustal contamination.
422 Instead, radiogenic isotopes from the Eocene volcanics suggest mixing between HIMU (high
423 $^{238}\text{U}/^{204}\text{Pb}$) and DMM (depleted mid-ocean ridge basalt mantle) mantle reservoirs, similar to many
424 of the Atlantic Ocean intraplate volcanoes (Mazza et al., 2014). The Eocene diatremes and some
425 of the dikes exhibit brecciated textures, carbonate inclusions within phenocrysts, and irregular
426 carbonate and zeolite amygdules within the volcanic groundmass (Haynes et al., 2014; Tso &
427 Surber, 2006), indicating the importance of volatiles in driving the Eocene eruptions. This is
428 consistent with high (>500 ppm) structural OH measured in clinopyroxene phenocrysts from
429 Highland County (Soles et al., 2014).

430 The structural features and petrography of the Eocene and Late Jurassic igneous bodies and
431 their xenoliths add to the regional context of the magmatism. Both pulses of magmatism were low

432 volume and exposed intrusive bodies vary from dikes ~10 cm in width to diatreme conduits ~200
433 m across. The Late Jurassic igneous rocks manifest as dikes that are preferentially oriented NW-
434 SE, approximately perpendicular to the strike of regional folding (Southworth et al., 1993). The
435 Eocene magmas produced dikes and diatreme structures (Haynes et al., 2014; Tso & Surber, 2006)
436 that align with jointing and faulting within the host sedimentary units, predominantly trending to
437 the NE-SW. The Eocene magmas are preferentially intruded into shale and carbonate units, though
438 sandstone xenoliths within the basalts at Trimble Knob and Mole Hill indicate that some eruptions
439 were able to punch through subsurface sandstone layers within duplex thrust splays or fold hinges
440 (Johnson et al., 2013; Tso & Surber, 2006). Phenocrysts, xenocrysts, and xenoliths reveal
441 information about the composition and temperature of the crust and lithospheric mantle.
442 Clinopyroxene phenocrysts and xenocryst rims from the Eocene event record pressures
443 corresponding to ~40 km depth, with temperatures ranging from 1230-1370°C (Johnson et al.,
444 2013), which agrees with other calculations that indicate the Eocene event sampled the
445 asthenospheric mantle. Paragneiss and syenite xenoliths are only confirmed to be found in Late
446 Jurassic dikes. Paragneissic xenoliths experienced temperatures as high as 984°C from Zr-in-rutile
447 thermometry and are of Grenville age, based upon detrital U-Pb zircon geochronology (Johnson
448 et al., 2013).

449 The two post-rifting magmatic events that affected the Central Appalachians thus likely
450 derived from the asthenospheric mantle at similar depths, but sampled geochemically distinct
451 sources. The Late Jurassic event sampled a highly-enriched mantle domain that is similar to other
452 magmatic events that effected the eastern margin of North America during the Late Jurassic (e.g.
453 New York kimberlites), suggesting that this event might be associated with widespread
454 magmatism. In addition, fractional crystallization of the more silica rich magmas occurred at the

455 base of the crust. On the other hand, the Eocene event shares geochemical and radiogenic isotopic
456 signatures of typical Atlantic intraplate volcanism with limited to no crustal interaction. The silica
457 rich magmas from the Eocene event evolved via fractional crystallization in the shallow crust.

458

459 **4. Geomorphological constraints**

460 Whether the present-day elevation and topographic relief along the Appalachian Mountains
461 represent continual, slow decay of remnant orogenic topography (e.g., Hack, 1960; Matmon et al.,
462 2003; Spotila et al., 2004) or reflect renewed rock uplift during the Cenozoic (e.g., Davis, 1889;
463 Pazzaglia & Brandon, 1996) remains a central question in the evolution of eastern North America.
464 Most workers agree that variations in the resistance of lithologic substrate to erosion along the
465 range manifest as differential landscape relief and rates of erosion (i.e., DiBiase et al., 2018; Hack,
466 1960; Hancock & Kirwan, 2007). However, variations in the pace of sediment delivery (Naeser et
467 al., 2016; Pazzaglia & Brandon, 1996), low-temperature thermochronology (Shorten and
468 Fitzgerald, 2020), the regional patterns of knickpoints preserved along some Appalachian river
469 networks (Gallen et al., 2013; Miller et al., 2013), and inverse models of stream profiles (Fernandes
470 et al., 2019) all imply that topographic relief increased during the late Cenozoic. Moreover, the
471 geodynamics driving such a change remain debated. For instance, in the Susquehanna River
472 watershed, north of our study area, regions of elevated channel steepness (a metric of channel
473 gradient normalized for basin drainage area; Wobus et al., 2006) and erosion rate were interpreted
474 to reflect an increase in river incision during the Neogene (Miller et al., 2013), perhaps reflecting
475 an increase in dynamic topography (Moucha et al., 2008; Moucha & Ruetenik, 2017; Rowley et
476 al., 2013). Similar patterns in topography and channel steepness in tributaries of the Tennessee
477 River, south of our study area, have been attributed to epirogeny (Gallen et al., 2013) but can also

478 be explained by river capture and drainage reorganization within approximately the same time
479 period (Gallen, 2018). These data were subsequently claimed to be consistent with dynamic
480 subsidence of the region driven by large-scale mantle flow (Liu, 2014). As our study area lies
481 between these two regions, the geomorphology of the range affords an opportunity to explore the
482 association between lithospheric architecture and potential changes in relief.

483 The high topography of the Appalachian Mountains above the CAA is characterized by
484 elevated channel steepness, relative to the Appalachians north and south, forming a broad
485 “bullseye” centered on the CAA, extending from southern West Virginia to the Pennsylvania
486 border (Figure 7A). Although the association of steeper channels with greater relief is not
487 surprising (e.g., DiBiase et al., 2010), elevated channel steepness indices along the crest of the
488 range are observed along both sides of the continental drainage divide (Figure 7D). This
489 observation suggests that elevated channel steepness is not simply a function of drainage capture
490 and divide migration (e.g., Naeser et al., 2016), but is characteristic of headwater regions of rivers
491 draining to both the Atlantic and Gulf of Mexico. Moreover, analysis of channel steepness as a
492 function of mapped lithology (see Supporting Information) reveals that channels are approximately
493 2-3 times steeper along the crest of the range, relative to its flanks, independent of substrate (Figure
494 7D). For instance, basins underlain by largely mudstone are present throughout a swath sampled
495 across the CAA (Figure 7D), and channels in these basins exhibit steepness indices of $\sim 20\text{-}25 \text{ m}^{0.9}$
496 near the crest of the range, decreasing to values $< 5\text{-}10 \text{ m}^{0.9}$ east and west of the range. This
497 observation suggests that variations in channel steepness are not entirely a consequence of
498 variations in rock erodibility along the range.

499 To evaluate whether these spatial differences in channel steepness are in fact associated
500 with differences in erosion rate, we compiled previously published data on basin-wide average

501 erosion rates from studies of ^{10}Be concentrations in fluvial sediment from tributaries of the
502 Potomac, James, and Susquehanna watersheds (Duxbury et al., 2015; Portenga & Bierman, 2011;
503 Portenga et al., 2019). For each of these watersheds, we evaluated the network distribution of
504 channel steepness (following methods of Harkins et al., 2007 and Perron & Royden, 2013) and
505 substrate lithology from published regional geologic maps (Dicken et al., 2005; Nicholson et al.,
506 2005). We focused our study on those 63 watersheds underlain by a single substrate lithology
507 (Table S1). We compared channel steepness to erosion rate for each watershed (Figure S1);
508 channel profiles that displayed significant convexities and knickpoints, considered to reflect
509 potential transient, spatial variations in erosion rate (e.g., Kirby & Whipple, 2012), were eliminated
510 from subsequent analysis. A detailed discussion of methods is available in the Supplemental
511 Information. The remainder of the data define two distinct scaling trends between erosion rate and
512 channel steepness (Figure 7B). Watersheds underlain by metabasalt and quartzite appear to be
513 steeper, at a given erosion rate, than those underlain by metasedimentary and sedimentary rocks
514 (Figure 7B). This analysis strongly implies that variations in channel steepness across the central
515 Appalachians (background colors in Figure 7A) in the study area do, in fact, reflect variations in
516 erosion rate. Steeper channels above the CAA appear to be eroding faster than the flanks of the
517 range (Figure 7).

518 Overall, elevated rates of erosion along steep channels in the central Appalachians appear
519 to be consistent with either: 1) maintenance of topography by ongoing differential rock uplift
520 across the range, and/or 2) relatively slow decay of erosion rates from a past event that may have
521 added buoyancy to the upper mantle and elevated the central Appalachians. Although our data are
522 not sufficient to definitively discriminate between these scenarios, we can estimate the response
523 timescales of a stream-power model of these fluvial networks (e.g., Goren et al., 2014). Although

524 such models are subject to significant limitations in how they represent the effects of stochastic
525 distributions of runoff and thresholds associated with bed sediment caliber (e.g., DiBiase &
526 Whipple, 2011; Lague, 2014), the linear scaling between channel steepness and erosion rate
527 presented here (Figure 7) suggests that stream-power type models capture at least the first-order
528 characteristics of the system. The linear scaling between channel steepness and erosion rate yields
529 a response time (τ) with the formula (Gallen, 2018; Goren et al., 2014)

$$530 \quad \tau = \int_0^{x'} \frac{dx'}{K(x')A(x')^m} \quad (3)$$

531 where x' is the along-stream distance from the outlet, K is an erosion coefficient, A is upstream
532 drainage area, and m is a positive exponent related to the scaling of erosion rate with drainage area,
533 a proxy for discharge. To estimate the response time for the Potomac River basin, we used two
534 spatially-variable erosion coefficients, estimated as the inverse of the regressions (see Supporting
535 Information) relating channel steepness and erosion rate (Figure 7). We applied those coefficients
536 to other rock types not included in the erosion rate analysis because such data in those rock types
537 are absent (e.g., including carbonates in the more erodible, higher K class and igneous rocks and
538 remaining metamorphic rocks in the less erodible, lower K class). In this way, our analysis honors
539 the observation that the scaling of channel steepness depends on lithology (Figure 7D), although
540 it does not specify every rock type. The exponent m was set to 0.45, consistent with both theory
541 (Whipple & Tucker, 1999) and observation in the Susquehanna River basin (Miller et al., 2013).
542 For rivers of the approximate size of the Potomac, our analysis suggests that the response to a
543 simple perturbation in the relative rate of base level fall would sweep through the system within
544 20-30 Myr. Thus, while it is possible that elevated erosion rates and steep channels reflect
545 modifications of the lithosphere associated with the youngest phase of volcanism in Eocene time,

546 it seems unlikely that the geomorphology of this region of the Appalachians retains any signal of
547 topographic changes that pre-date these events.

548

549 **5. Synthesis of observations: An argument for lithospheric loss beneath the Central** 550 **Appalachians**

551 Taken together, the constraints from geophysics, petrology, geochemistry, and
552 geomorphology described in Sections 2-4 form a suite of observations that suggest a past
553 lithospheric loss event(s) and the preservation of a thinned continental lithosphere through
554 geologic time. Our synthesis has documented a number of striking and anomalous observations
555 associated with the CAA that any conceptual model for lithospheric evolution must be able to
556 explain. To summarize, a number of geophysical imaging studies (Figures 2 and 3) have
557 conclusively demonstrated that the lithosphere beneath the Central Appalachian Anomaly today is
558 thin, with the LAB likely at ~75-90 km depth. These constraints include 1) tomographic imaging
559 of low seismic velocities associated with the CAA, suggesting a region of absent lithosphere that
560 is no wider than ~100 km and with low velocities extending to the base of the continental crust, 2)
561 seismic attenuation measurements, which again suggest a region of thin lithosphere of limited
562 lateral extent, 3) electrical conductivity measurements that require a shallow LAB and a highly
563 conductive asthenosphere co-located with the tomographically imaged CAA, 4) Sp receiver
564 function imaging, which suggests a shallow LAB that is spatially associated with the electrical
565 conductivity anomaly, and is consistent with geochemically constrained asthenospheric melting
566 depths.

567 The physical state of the upper mantle associated with the CAA today is therefore relatively
568 clear – a thin lithospheric layer overlies an asthenosphere with geophysical indicators that are in

569 some ways more typical of mid-ocean ridge settings than ambient subcontinental asthenosphere.
570 Resistivities below ~100 km depth are less than 10 Ωm (Evans et al., 2019), which is more
571 conductive at comparable depths than beneath unmodified oceanic lithosphere (Sarafian et al.,
572 2015) and comparable to asthenosphere beneath the East Pacific Rise at similar depths (Baba et
573 al., 2006a,b; Key et al., 2013). The strength of attenuation is likewise comparable to that beneath
574 the Juan de Fuca ridge (Eilon & Abers, 2017), or Lau (Wei & Wiens, 2018, 2020) and Marianas
575 (Pozgay et al., 2009) back-arc spreading systems. Shear-wave velocities as constrained by surface
576 waves are typically in the range of ~4.3-4.5 km/s at depths below 150 km beneath the CAA (Pollitz
577 & Mooney, 2016; Porter et al., 2016; Shen & Ritzwoller, 2016; Wagner et al., 2018); these are
578 more consistent with the asthenosphere beneath young oceanic plates than the continents (e.g.,
579 Lekic & Romanowicz, 2011). Taken together, the geophysical observations suggest the CAA
580 comprises a region of partial melt at shallow depths below the continental crust over a very small
581 (50 km radius) area.

582 The fact that these geophysical indicators of a region of absent mantle lithosphere and
583 shallow partial melt are spatially co-located with the occurrence of Late Jurassic and Eocene
584 volcanic and magmatic products (Figure 3) leads us to consider models that would explain both of
585 these past episodes of tectonomagmatism and the present-day geophysical structure in terms of
586 lithospheric loss and subsequent evolution. Key geochemical and petrological constraints that must
587 be honored by such models include 1) the timing of the events, with one during the Late Jurassic
588 and one during the Eocene, 2) the thermobarometry results, which suggest pressures (and thus
589 depths) of melt equilibration of 2.1 GPa (roughly 70 km) for a Late Jurassic sample and 2.3 GPa
590 (roughly 75 km) for Eocene samples, and temperatures that are associated with decompression
591 melting of “normal” asthenosphere, and 3) the geochemical results, which for the Eocene event

592 similarly suggest decompression melting of “normal” asthenosphere from the sub-Atlantic Ocean
593 domain. Finally, the fact that the anomalous magmatic activity and present-day geophysical
594 anomalies are spatially co-located with relatively rapid erosion rates and steep channels also
595 pushes us to consider models for evolution of the Central Appalachian lithosphere that can explain
596 particularly rapid present-day erosion rates.

597 In other words, all available observations are consistent with shallow decompression
598 melting caused by lithospheric removal in the Jurassic, followed by a ~100 Ma hiatus (about which
599 we know very little), followed by another episode of small-scale volcanism during the Eocene
600 (which may or may not have included additional lithospheric removal), followed by some process
601 that has allowed for the maintenance of low seismic velocities, high seismic attenuation, low
602 resistivity, and high erosion rates for 47 million years. This means that we need to explain a) the
603 removal of mantle lithosphere on such a small scale, and b) the maintenance of such a small
604 lithospheric “hole” over geologic time.

605 In addition to the key geophysical, geomorphological, geochemical, and petrological
606 observations that suggest anomalous lithospheric evolution, we have also documented a number
607 of additional observations that may help to distinguish among different models. These include the
608 occurrence of a transition in SKS splitting behavior that is co-located with the CAA, the Moho
609 “step” that is just to the east of the Eocene volcanics, the observation of relatively “normal” and
610 unexciting transition zone structure beneath the CAA, the lack of pronounced anomalies in the
611 gravity and heat flow data, and the lack of a pronounced seismic velocity anomaly in the crust
612 above the upper mantle CAA.

613

614

615 **6. Mechanisms for lithospheric loss and evolution beneath the Central Appalachians**

616 Here we discuss and evaluate a range of possible conceptual models for a) lithospheric loss
617 (and associated intraplate volcanism) beneath our Central Appalachians study area, and b) the
618 evolution and maintenance of thin lithosphere over geologic time. Many of these ideas are based
619 on previous work that have suggested mechanisms for explaining various observations (for
620 example, low upper mantle seismic velocities, or the character and timing of volcanism). Section
621 6 focuses on a description of possible models, and Section 7 presents a comparison between
622 predictions and observations. At this point, our evaluations of the various mechanisms are
623 qualitative and conceptual; however, they represent a starting point towards more quantitative and
624 specific comparisons between a working preferred model and observations, as described below.

625

626 *6.1 Mechanisms for lithospheric loss*

627 *6.1.1 Localized loss via Rayleigh-Taylor instability*

628 Mazza et al. (2014) proposed a localized lithospheric loss or delamination model for the
629 central Appalachians as a mechanism to explain anomalous volcanism. This scenario invokes the
630 gravity-driven loss of a small volume of lithosphere via a Rayleigh-Taylor instability (e.g., Elkins-
631 Tanton, 2007; see sketch in Figure 8). We envision a localized (no more than ~100 km across,
632 roughly the dimension of the present-day low velocity anomaly at depths of ~100 km) Rayleigh-
633 Taylor instability of dense mantle lithosphere, perhaps also involving eclogitized, high-density
634 lower crustal material. This lithospheric “drip” would have been relatively small in volume (with
635 a diameter of ~100 km and a thickness of perhaps ~50-100 km, consistent with numerical modeling
636 results; e.g., Conrad & Molnar, 1997), and after it detached and sank into the upper mantle,
637 upwelling return flow would have resulted in decompression melting.

638

639 *6.1.2 Widespread lithospheric loss via Rayleigh-Taylor instability*

640 An alternative to the model of a localized gravity-driven lithospheric loss event is a
641 scenario in which a comparatively larger volume of lithospheric mantle was removed, with
642 subsequent thermal evolution (as discussed in section 6.2.1 below) that shrank the region of
643 thinned lithosphere to its present size. Such a scenario, to which the term “lithospheric
644 delamination” is often applied (e.g., Magni & Király, 2020), raises the possibility that a
645 substantially larger portion of the mantle lithosphere was initially lost than envisioned in section
646 6.1.1 above. Our motivation for considering this idea is that in this scenario there is no need to
647 invoke a set of processes that maintain the configuration of the lithosphere that was created by the
648 most recent lithospheric loss event over long periods of geologic time. Instead, we envision that
649 after the lithospheric loss event, the lithosphere progressively cooled and thickened; in the course
650 of this evolution, what was initially a larger lithospheric “divot” shrank to its present dimensions.

651

652 *6.1.3 Gradual thinning of the lithosphere via thermal ablation*

653 Evans et al. (2019) suggested a model of gradual, rather than a catastrophic, lithospheric
654 loss beneath the Central Appalachians as a possible alternative to gravity-driven instability. We
655 envision a scenario in which some initial perturbation of the “topography” at the base of the
656 lithosphere, perhaps tied to preexisting or inherited lithospheric structure from earlier processes,
657 allowed for the localization of upwelling mantle flow and the progressive thermal ablation or
658 erosion of the lithosphere to its present-day configuration. Evans et al. (2019) invoked the idea of
659 shear-induced upwelling as a possible mechanism for this process; if variable topography on the
660 lithosphere, and/or lateral variations in mantle viscosity, led to shear-driven upwelling (e.g.,

661 Ballmer et al., 2015; Conrad et al., 2010, 2011), then any melt produced would migrate to the
662 shallowest point of the LAB. Melt ponded at the LAB may then play a role in thermally eroding
663 the lithosphere via dike intrusion (e.g., Havlin et al., 2013); this model predicts that over time, the
664 lithosphere progressively erodes and evolves to its present-day configuration. This model does
665 not make specific predictions about the time frame of the gradual lithospheric thinning, and the
666 timescale over which this may have occurred is not well constrained. Havlin et al. (2013) suggested
667 that this type of mechanism, with modest melt fractions, can thin the lithosphere by roughly 50 km
668 or more over a 50 Myr time frame.

669

670 *6.1.4 Lithospheric thinning via edge-driven convection*

671 Another possibility is that the present-day low velocities beneath the Central Appalachians
672 represent the upwelling limb of a small-scale convection cell that is driven by downwelling at the
673 edge of the thick portion of North American cratonic lithosphere to the west. This model invokes
674 the classic edge-driven convection scenario of King and Anderson (1998) and King (2007), which
675 has been considered before in a slightly different context as an explanation for processes occurring
676 beneath the southeastern U.S. (Benoit et al., 2013; Long et al., 2010). The concept of edge-driven
677 convection has been applied to explain lithospheric thinning and intraplate volcanism in other
678 geographic settings (e.g., Kaislaniemi & van Hunen, 2014; Van Wijk et al., 2010), and has also
679 been invoked to explain the Northern Appalachian Anomaly, another low-velocity upper mantle
680 anomaly associated with thinned lithosphere that is centered under New England (e.g., Dong &
681 Menke, 2017; Levin et al., 2018; Menke et al., 2016, 2018). In this model, the upwelling limb of
682 the convection cell causes decompression melting and corresponds to the present-day low velocity
683 anomaly in the upper mantle; the upwelling may have contributed to lithospheric thinning over

684 time through thermal ablation, yielding the thin lithosphere that is inferred today. While this model
685 is not temporally specific in the same way that the catastrophic lithospheric loss is, the edge-driven
686 convection cell may have been present continuously (or at least episodically) for long periods of
687 geologic time if it is to be invoked as an explanation for past intraplate volcanism in our study
688 region.

689

690 *6.1.5 Lithospheric thinning driven by a deep, plume-like upwelling*

691 Yet another plausible scenario invokes deep processes, rather than processes taking place
692 in the upper mantle, as the driver for melting and volcanism beneath the Central Appalachians.
693 This model invokes the presence of an anomaly in the mid-mantle (or deeper) as the trigger for
694 melting and as the explanation for the present-day low velocity zone and thin lithosphere. This
695 anomaly could take the form of a classical thermal mantle plume, which may have been able to
696 thermally ablate or thin the lithosphere when it passed through. Alternatively, it could take the
697 form of a “wet spot” whose increased water content lowers the melting temperature and enables
698 melting, and may contribute directly to the reduced seismic velocities in the upper mantle. Each
699 of these two scenarios has been previously proposed in the literature. Chu et al. (2013) proposed
700 the presence of a “hidden hotspot track” beneath the central and Eastern U.S. on the basis of
701 seismic waveform modeling that suggested two corridors of modified lower lithosphere with
702 reduced seismic velocities and enhanced seismic attenuation. Van der Lee et al. (2008) previously
703 suggested pervasive hydration of the upper mantle beneath eastern North America on the basis of
704 documented low-velocity anomalies beneath the Eastern Seaboard in tomographic models that
705 predate the deployment of the EarthScope USArray (e.g., Van der Lee & Frederiksen, 2005). In
706 the Van der Lee et al. (2008) model, hydration and upwelling were invoked to explain a broad

707 region of lower than average upper mantle velocities beneath the eastern U.S.; in contrast, here we
708 invoke the possibility of a much narrower and more localized hydrous upwelling as a source of
709 melt production directly beneath the Central Appalachians.

710

711 *6.2 Scenarios for evolution of thinned lithosphere over time*

712 We envision several possible scenarios for how the lithosphere may have evolved after a
713 lithospheric loss event by any of the mechanisms discussed in section 6.1. These models may
714 include gradual thermal healing of thinned lithosphere (perhaps accompanied by temporal changes
715 in density structure) or mechanisms that can maintain a thin lithosphere over time, including shear-
716 driven upwelling or continuous or episodic edge-driven convection.

717

718 *6.2.1 Gradual thermal healing of thinned lithosphere*

719 The simplest and most straightforward idea for the temporal evolution of the lithosphere
720 after an episode of lithospheric loss or removal is the gradual healing or re-forming of the
721 lithospheric mantle through time. While a lithospheric loss event would likely be accompanied by
722 upwelling and perhaps heating of the base of the of the lithosphere, over time one might expect
723 the continental lithosphere to thicken and densify as it progressively cools, much as oceanic
724 lithosphere evolves as it ages and moves away from the mid-oceanic ridge. In addition to the
725 increase in density expected as the lithosphere cools, changes in its density structure due to
726 metamorphic reactions (e.g., Fischer, 2002) are also possible. We would generally expect that a
727 mechanism of thermal healing would slowly thicken the lithosphere over time, causing an initial
728 “hole” or “divot” to gradually disappear through progressive thickening.

729

730 *6.2.2 Maintenance of thinned lithosphere via small-scale mantle flow and shear-driven upwelling*

731 If one or more lithospheric loss events took place beneath the central Appalachians in the
732 geologic past, then a potential mechanism is needed to maintain the thinned lithosphere over
733 geologic time (rather than allowing for thermal healing via the slow regrowth of lithosphere
734 through gradual cooling). Small-scale mantle flow driven by the motion of the North American
735 Plate may have played a role in maintaining the “hole” or “divot” in the lithosphere. One possibility
736 is that as the plate continued to move over the asthenospheric mantle beneath it, it induced a small-
737 scale mantle flow cell within the divot itself (see Figure 8), continuously bringing relatively hot
738 asthenospheric upper mantle into contact with the base of the lithosphere and preventing thermal
739 healing of the lithospheric divot. This idea is similar to the concept of shear-driven upwelling as a
740 mechanism to produce melting and volcanism in intraplate settings (Conrad et al., 2010, 2011).

741

742 *6.2.3 Maintenance of thinned lithosphere via continuous or episodic edge-driven convection*

743 As discussed in section 6.1.4, edge-driven convection has been suggested as a possible
744 mechanism to explain volcanism in the Central Appalachians and in other intraplate settings. Edge-
745 driven convection may be more or less continuous, with nearly continuous downwellings initiated
746 at the base of the thick continental lithosphere near its edge, or it may be episodic, with an abrupt
747 episode of downwelling (accompanied by upwelling return flow on the other limb of the
748 convection cell) followed by a period of quiescence and ultimately another pulse of mantle flow
749 (perhaps associated with an abrupt change in plate motion). If edge-driven convection is present
750 beneath the Central Appalachians, then it may have played a role in maintaining a relatively thin
751 lithosphere over long periods of time through multiple episodes of downwelling, upwelling return

752 flow, and lithospheric thinning, or through a continuous (or nearly continuous) version of this
753 process.

754

755 **7. Which models are most consistent with the observations?**

756 *7.1 Mechanisms for lithospheric loss and evolution: Comparison with observations*

757 *7.1.1 Lithospheric loss via localized gravity-driven instability*

758 Lithospheric loss via a relatively small gravity-driven Rayleigh-Taylor instability during
759 the Eocene (and perhaps also during the Jurassic, if the loss was episodic) is generally consistent
760 with many of the observations. Specifically, this mechanism is compatible with the primitive
761 composition and estimated depths and temperatures of melt equilibration of the Eocene magmatic
762 products, as argued by Mazza et al. (2014). It is also consistent with the observations of the present-
763 day upper mantle anomalies in seismic velocities, seismic attenuation, and electrical conductivity
764 (Figure 3). All of these indicators, along with the Sp receiver function imaging, are consistent with
765 thin lithosphere beneath the Central Appalachians, directly beneath the Eocene volcanic and
766 magmatic products at the surface. This mechanism can explain the small size and the spatial
767 location of the upper mantle anomalies, in that the present-day lithosphere is thin in the region
768 where a small volume of lithosphere was presumably lost during the Eocene.

769 If a small volume of lithosphere were removed via gravitational instability during the
770 Eocene, then we might consider whether we might expect to image a lithospheric fragment in the
771 mantle transition zone. Given its small dimensions (~50 km radius), any detached lithosphere
772 should have thermally equilibrated with the surrounding asthenospheric mantle fairly quickly as it
773 sank. Specifically, the timescale for heat to diffuse over a distance, d , is given by

774
$$t_d \sim \frac{d^2}{4\kappa} \quad (4)$$

775 where κ is the thermal diffusivity, which for the mantle is $\sim 10^{-6} \text{ m}^2 \text{ s}^{-1}$. A sphere of lithosphere
776 with 50 km radius would thus thermally equilibrate with the surrounding asthenospheric mantle
777 on the order of 20 Myr. The observed lack of strong topography on the mantle transition zone
778 discontinuities beneath the Central Appalachians (Figure 4) can therefore be considered as
779 consistent with lithospheric loss via Rayleigh-Taylor instability during the Eocene (and/or earlier).

780 The length and time scales of lithospheric Rayleigh-Taylor type instabilities have been
781 estimated by Conrad & Molnar (1997). Including the effect of thermal diffusion, instabilities grow
782 most rapidly at wavelengths on the order of 100-200 km. Assuming an asthenospheric viscosity of
783 10^{19} Pa s , the instabilities grow by a factor of e every 3-5 Myr. Because such instabilities only
784 displace the bottom one third to one half of the lithosphere (e.g., Conrad & Molnar, 1997), these
785 instabilities would produce only small anomalies in topography and gravity at the Earth's surface
786 above the downwelling, consistent with the (lack of) observations.

787 The region of inferred lithospheric loss is just to the west of the sharp step in the Moho,
788 but possible links between them remain unclear. The particularly thick crust (~ 50 -55 km; Long et
789 al., 2019) beneath the Central Appalachian Mountains (Figure 3) may point to the presence of
790 unusually dense, perhaps eclogitized, material in the lower crust today. There is some additional
791 support for the idea of particularly dense lower crust, at least during the Late Jurassic, from the
792 observation of xenoliths of garnet-rich gneisses in the lower crust, found in Late Jurassic magmas
793 (Johnson et al., 2013). It is unclear, however, whether such material may have been present in the
794 geologic past and whether it may have played a role in triggering the Rayleigh-Taylor instability
795 through which the lithosphere was lost. If eclogitized lower crustal material was involved in the
796 episode of lithospheric loss during the Eocene, then that might suggest that the crust beneath the
797 mountains was even thicker in the geologic past.

798 It is not clear whether the observed elevated rates of present-day erosion in the Central
799 Appalachians (Figure 7) might be directly associated with an episode of lithospheric removal
800 during the Eocene. If a Rayleigh-Taylor instability removed a portion of dense lithosphere and
801 therefore adjusted the overall buoyancy of the system during the Eocene, then uplift and enhanced
802 erosion would be expected. It is unclear, however, whether the present-day erosion rates would be
803 expected to still reflect this event, given the timescales involved. As discussed in section 4, simple
804 scaling arguments suggest that the timescales of response for the rivers draining the Central
805 Appalachians today are no greater than ~30 Ma. Unless any pulse of enhanced uplift and erosion
806 has decayed more slowly than expected (c.f. Baldwin et al., 2003), it is difficult to directly link
807 elevated present-day erosion rates with an episode of lithospheric loss during the Eocene. An
808 indirect link may be possible, however, if the lithospheric divot is being maintained via small-scale
809 mantle flow today, as discussed further in 7.1.6 below.

810 While Mazza et al. (2014) proposed a lithospheric loss scenario to explain Eocene
811 volcanism, it is possible that there were in fact multiple episodes of catastrophic lithospheric loss
812 beneath the region, perhaps corresponding to both the Jurassic and Eocene volcanic pulses. One
813 possibility is that some aspect of lithospheric structure beneath the Central Appalachians has made
814 it particularly prone to gravitational instability – perhaps related to lithospheric weakening, or to
815 its density structure – that may have been created or “seeded” during the breakup of Pangea. A
816 possible scenario is that a Rayleigh-Taylor instability led to the loss of lithosphere in the Late
817 Jurassic, causing upwelling return flow and decompression melting, and leading to magmatic
818 activity at the surface (Mazza et al., 2017). This event may well have modified the structure of the
819 crust and/or remaining lithospheric mantle, and may have emplaced particularly dense material
820 (i.e., underplated mafic rocks) at the base of the crust, perhaps priming the system for another,

821 later phase of lithospheric loss. Between the Late Jurassic and the Eocene, the structure of the
822 lithosphere may have evolved and been modified via thermal healing; furthermore, the density
823 structure of the deep crust may have evolved, perhaps through time-progressive metamorphic
824 reactions (e.g., Fischer, 2002; Williams et al., 2014). As the system evolved through time, the
825 lithosphere beneath the Central Appalachians may have become more gravitationally unstable,
826 perhaps via a combination of the changing density structure (as the lithosphere cooled) and through
827 preexisting factors such as the presence of low-viscosity lithosphere (either from the tectonic
828 inheritance of preexisting weak zones, the presence of volatiles such as water, or other factors).
829 This may have led to a second lithospheric loss event during the Eocene, which led to a similar
830 scenario of upwelling return flow, the production of partial melt, and the transport of that melt
831 through the overlying crust to the surface.

832

833 *7.1.2 Gradual lithospheric thinning via thermal ablation*

834 A gradual lithospheric thinning mechanism could also be considered as generally
835 consistent with the imaging of the present-day lithospheric structure beneath the Central
836 Appalachians. Such a mechanism can explain the size and location of the upper mantle anomalies
837 in seismic velocity, attenuation, and electrical conductivity; in particular, this model, which
838 appeals to the ponding of melt at the shallowest point of the lithosphere as it gradually thins, is
839 consistent with the inference from both electrical conductivity and attenuation measurements that
840 partial melt may be present in the shallow asthenosphere today. Furthermore, this mechanism may
841 provide a natural explanation for the persistence of the lithospheric divot over geologic time
842 (without needing to appeal to a process such as edge-driven convection to maintain it).

843 On the other hand, a mechanism that invokes gradual thinning cannot explain the temporal
844 specificity of the Late Jurassic or Eocene volcanism. In the context of this mechanism, additional
845 processes (such as the reactivation of crustal structures and/or the reorganization of the crustal
846 stress field) must be invoked to explain the timing of pulses of volcanic activity. Interestingly, the
847 bend in the Hawaii-Emperor seamount change suggests a global reorganization of plate motions
848 at roughly ~47 Ma (e.g., Wright et al., 2015); while this is speculative, in the context of this model
849 this global change may have reorganized the stress field in our study region and allowed for the
850 migration of melt to the surface (e.g., Southworth et al., 1993). This would mean that the
851 lithospheric geometry seen today may have been established in the Jurassic (producing the initial
852 episode of magmatism) and may have changed little since that time. In this framework, the Eocene
853 volcanism only occurred due to a passing favorable re-organization of stresses and associated
854 opening of crustal magmatic conduits, or due to a transient episode of more intense upwelling and
855 melt production associated with a change in plate motion. (It is worth noting that this idea may
856 apply regardless of the mechanism for lithospheric removal during the Jurassic, whether it was
857 catastrophic or gradual.)

858 Gradual thinning of the lithosphere would predict that the equilibration depths of mantle-
859 derived melts should decrease over time; however, this prediction is not particularly well borne
860 out by petrological observations. Specifically, Mazza et al. (2017) found an equilibration pressure
861 of 2.09 GPa (roughly 70 km) for a Late Jurassic sample (Sample #31), compared with equilibration
862 pressures of 2.32 ± 0.31 GPa for Eocene samples (Mazza et al., 2014). We note, however, that
863 direct comparisons are difficult, because data for the Late Jurassic are limited; most of the Late
864 Jurassic samples are highly alkaline, precluding the use of traditional geothermobarometers due to
865 the mineralogy and magma composition (Mazza et al., 2017).

866

867 *7.1.3 Widespread lithospheric loss with subsequent healing/regrowth*

868 A mechanism of widespread lithospheric loss (that is, a Rayleigh-Taylor instability whose
869 dimensions were significantly larger than the present-day upper mantle geophysical anomaly)
870 could be generally consistent with the timing and petrological characteristics of Central
871 Appalachian volcanism, but not their spatial localization. Specifically, if a large volume of
872 lithosphere had been removed, then volcanism over a wider region would be expected; instead, the
873 expression of Eocene magmatism at the surface is localized to a small region of western Virginia
874 and eastern West Virginia (Figure 1). This mechanism also does not provide a particularly specific
875 explanation for the location of the present-day upper mantle velocity, attenuation, and conductivity
876 anomalies, or for their co-location with the Eocene volcanics. We can conjecture that the present-
877 day location of the CAA corresponds to the center of the region of lithospheric loss (that is, where
878 the thickest column of lithosphere was removed), but this is speculative. This model is generally
879 difficult to reconcile with constraints provided by modeling studies of Rayleigh-Taylor instabilities
880 (e.g., Conrad & Molnar, 1997), which suggest that long-wavelength instabilities would create
881 surface deformation; evidence for this is not observed. Furthermore, if a large amount of material
882 was removed during a past episode(s) of lithospheric loss, we might expect to be able to observe
883 it as a high-velocity anomaly in the mantle today (for a spherical anomaly with a radius of ~500
884 km, the thermal diffusion time would be roughly 2 Gyr), and we do not.

885 One aspect of the observations that could potentially be explained by this mechanism is the
886 inference of altered mantle lithosphere just to the west of the upper mantle conductivity anomaly,
887 as discussed by Evans et al. (2019). They hypothesized that the mantle lithosphere here has
888 undergone alteration due to deformation via shearing or through hydration, leading to higher

889 conductivity values than is expected for typical continental mantle lithosphere (such as those
890 observed further to the west along the MAGIC profile). It is possible that these alteration processes
891 may reflect the evolution of the mantle lithosphere through healing and thermal regrowth, if this
892 portion of the lithosphere was included in a hypothetical larger lithospheric loss event. However,
893 lithosphere would generally be expected to thermally heal from the top down, rather than laterally,
894 making it somewhat difficult to envision how an initially large area of thinned lithosphere might
895 shrink in lateral extent (that is, in map view) while maintaining a shallow LAB. It is thus difficult
896 to envision a physically reasonable mechanism for the evolution of a past large lithospheric divot
897 or hole to the configuration that we image today.

898

899 *7.1.4 Edge-driven convection*

900 An edge-driven convection mechanism for lithospheric thinning (and/or the maintenance
901 of thin lithosphere through geologic time) fails to match the observations beneath the Central
902 Appalachians in several key aspects. This model does not easily explain the temporal specificity
903 of the Late Jurassic or Eocene magmatic activity, unless episodic edge-driven convection is
904 invoked, and even then, it is not easy to reconcile the persistence of the geophysical anomalies into
905 the present day unless other processes are involved. Edge-driven convection is also not easily
906 reconciled with the spatial localization of both the magmatic pulses and the present-day
907 geophysical anomalies in the upper mantle; if small-scale convection driven by downwellings at
908 the edge of the thick North American cratonic lithosphere to the west is driving upwelling and
909 volcanism beneath the Central Appalachians, then why do we not observe intraplate volcanism
910 and upper mantle anomalies everywhere along the margin? (One possibility, of course, is that the
911 vigor and/or periodicity of edge-driven convection may vary along strike; previous work (e.g., Till

912 et al., 2010) has shown that the size of the edge-associated downwelling depends on the sharpness
913 of the edge, so along-strike variability in edge-driven convection could reflect along-strike
914 differences in lithospheric architecture.)

915 If edge-driven convection were active today beneath the Central Appalachians, we would
916 expect upwelling in the upper mantle beneath our study area; the vertical shearing produced by
917 such an upwelling should produce vertically oriented fast axes of seismic anisotropy and would
918 therefore predict negligible shear wave splitting stemming from anisotropy in the asthenospheric
919 upper mantle. This is not obviously consistent with the SKS splitting observations in our study
920 region (Figure 3), which exhibit a modest rotation in fast splitting directions near the Central
921 Appalachian Anomaly but no significant local minimum in splitting delay times. Of course, this
922 prediction could be complicated by the presence of anisotropy in the mantle lithosphere; however,
923 the thin (~80 km) lithosphere that is present beneath the Central Appalachians implies that a
924 significant contribution to SKS splitting from the asthenospheric upper mantle is likely (Aragon
925 et al., 2017). We further acknowledge that flow patterns in the mantle are likely to be complex and
926 even in areas of upwelling, the regions of null SKS splitting may be spatially restricted (e.g.,
927 Blackman & Kendall, 2002), so comparisons between SKS splitting and predictions for edge-
928 driven convection models are not straightforward.

929 The predictions that the edge-driven convection model would make about transition zone
930 structure are a bit ambiguous. If an edge-driven convection cell exists today and is confined to the
931 upper mantle, then we would expect no effect on the mantle transition zone discontinuities.
932 However, if a present-day convection cell is larger and the mantle flow associated with it penetrates
933 the mantle transition zone, then we might expect to see a localized thinning of the transition zone
934 beneath the Central Appalachians. Data from the MAGIC array indicate no such localized thinning

935 (Figure 4), and studies based on USArray TA data mostly argued against transition zone thinning
936 beneath our study region (Liu & Gao, 2014; Wang & Pavlis, 2016), although Keifer and Dueker
937 (2019) did find some evidence for a thin transition zone beneath the Central Appalachians.

938

939 *7.1.5 A deep thermal or hydrous mantle anomaly*

940 A mechanism for lithospheric thinning that invokes a deep source of heat (via a thermal
941 mantle plume) and/or hydration makes some specific predictions about mantle structure that are,
942 for the most part, not borne out by the observations. There is little or no evidence for a deep mantle
943 plume, or for a localized conduit of particularly hydrated mantle that is connected to a source in
944 the deep mantle, in images of present-day mantle structure. While the Central Appalachian upper
945 mantle velocity anomaly is a robust feature in most tomography models (Figures 2 and 3), there is
946 little or no evidence that it is connected to slow structures in the transition zone or lower mantle
947 (e.g., Biryol et al., 2016).

948 A model of a thermal or hydrous plume conduit that is fed by the deep mantle and remains
949 stationary in a mantle reference frame while the North American plate moves above it is also
950 difficult to reconcile simultaneously with presence of geophysical anomalies in the shallow upper
951 mantle today and with magmatic activity during the Late Jurassic and Eocene. While a mantle
952 plume has been proposed as a possible explanation for intraplate volcanism in eastern North
953 America, including the Eocene volcanics (Chu et al., 2013), the motion of the North American
954 plate (absolute plate speed of ~34 mm/yr relative to the mantle beneath, in the hotspot reference
955 frame of the HS3-Nuvel 1A model; Gripp & Gordon, 2002) means that the present-day location
956 of the mantle plume would be roughly 1600 km to the east, and the upper mantle geophysical
957 anomalies would not be particularly well explained. Conversely, if the plume were located beneath

958 the Central Appalachians today, then it could be invoked as an explanation for the geophysical
959 anomalies but would not be a good explanation for the intraplate volcanism. The co-location of
960 the Eocene and Late Jurassic magmatic products with the present-day geophysical anomalies is
961 thus not easy to reconcile with the concept of a deep mantle source, unless one assumes that the
962 upper mantle geophysical anomalies were caused by the passage of a mantle plume in the past and
963 then have been maintained over time through other processes.

964 As with the edge-driven convection mechanism, a plume model would predict upwelling
965 flow in the upper mantle (if the plume were located beneath the Central Appalachians today),
966 which is not particularly consistent with the SKS splitting observations (Figure 3), although SKS
967 splitting patterns predicted by plume models are often complex and depend on a number of factors
968 (e.g., Ito et al., 2015). A model that invokes a hot or hydrous upwelling from the deep mantle
969 would also predict complexities in transition zone structure, including transition zone thinning (via
970 the depression of the 410 km discontinuity and the elevation of the 660 km discontinuity; e.g.,
971 Bina & Helffrich, 1994) if thermal effects dominate. As discussed by Long et al. (2010), a hydrous
972 transition zone such as that proposed by Van der Lee et al. (2008) would predict a shallowing of
973 the 410 km discontinuity of ~20-40 km under water-saturated conditions (Smyth & Frost, 2002),
974 producing ~20-40 km of transition zone thickening. Neither of these effects is observed; the
975 transition zone thickness beneath the MAGIC line (Figure 4) is close to the global average.

976

977 *7.1.6 Maintenance of thin lithosphere via shear-driven upwelling*

978 The idea that the lithospheric divot that is observed today results from one or more past
979 episodes of catastrophic (but relatively localized) lithospheric loss and has been maintained by
980 small-scale mantle flow and shear-driven upwelling due to the motion of the North American Plate

981 over the mantle beneath it makes a few predictions that can be tested with our observations. This
982 mechanism is generally consistent with the inference that there may be partial melt in the
983 uppermost mantle beneath the CAA today, as suggested by Evans et al. (2019) and Byrnes et al.
984 (2019), as ongoing shear-driven upwelling would result in a continuous process of decompression
985 melting. It may also be consistent with SKS splitting observations, in that it may provide an
986 explanation for the rotation in SKS fast splitting directions observed in western Virginia (Figure
987 3). Specifically, if the overall upper mantle flow field (likely dominated by plate-motion-parallel
988 shearing; e.g., Long et al., 2016; Yang et al., 2017) is being locally disturbed by small-scale flow
989 associated with shear-driven upwelling, then this may explain the local change in SKS splitting
990 behavior. While we do not observe the weak or absent SKS splitting that would be predicted for
991 truly vertical shearing over a substantial area (e.g., Levin et al., 2018; Long et al., 2010), the scale
992 of a possible shear-driven upwelling is likely small enough that we would not predict a clear
993 transition to null or absent splitting in the SKS data. (We caution that there are other ways to
994 explain the lateral variation in SKS splitting behavior, as it may plausibly be dominated by
995 contributions from frozen-in structure in the lithosphere, rather than present-day mantle flow.)

996 The notion of small-scale mantle flow that includes an upwelling component is also
997 generally consistent with the observation of elevated erosion rates along steeper channels in the
998 Central Appalachians today (Figure 7). The present-day scaling of erosion rate, channel steepness
999 and erosional efficiency for these rivers suggest a response timescale of ~30 Ma, which is less than
1000 the time elapsed since the last episode of volcanism during the Eocene. If the elevated rates of
1001 erosion instead reflect ongoing uplift or buoyancy from the upper mantle, then this would be
1002 broadly consistent with ongoing shear-driven upwelling associated with small-scale mantle flow
1003 within the lithospheric divot (Figure 8).

1004 One aspect of the present-day geophysical structure that is not explained well by a shear-
1005 driven upwelling mechanism to maintain the lithospheric divot is the velocity structure of the crust
1006 above the CAA (Figure 3). Specifically, the lack of a crustal low-velocity anomaly is puzzling, as
1007 one would expect the crust overlying the thinned lithospheric mantle to undergo warming over
1008 geologic time and to display lower velocities today if shear-driven upwelling of the asthenosphere
1009 has been continuously operating since at least the Eocene. Of course, if there was a compositional
1010 effect on crustal velocities in the region, with anomalously fast velocities due to compositional
1011 variations, then this effect could in theory offset a potential thermal effect.

1012

1013 *7.2 Preferred models for lithospheric evolution beneath the Central Appalachians*

1014 The comparisons between observations and the predictions of various mechanisms of
1015 thinning the lithosphere and maintaining thin lithosphere through time described in Section 7.1
1016 lead us to a small set of preferred models for the evolution of the Central Appalachian lithosphere
1017 since the breakup of Pangea. We emphasize that our preferred models are not perfect and are not
1018 completely consistent with the full range of observations. Furthermore, at this point our
1019 comparisons between model predictions and observations is almost entirely qualitative, and more
1020 specific, detailed, and quantitative modeling is needed in the future to link model predictions more
1021 definitively to observations. Despite these limitations, however, we can present a small set of
1022 favored models that are better able to match the observational constraints than others.

1023 Given the preponderance of the observational evidence, we see the scenarios illustrated in
1024 Figure 8 as being most consistent with the full range of available constraints. We suggest that there
1025 was an episode of lithospheric loss during the Late Jurassic, perhaps via a gravitationally driven
1026 Rayleigh-Taylor instability that removed a relatively small volume of lithosphere, or perhaps due

1027 to another process such as thermal ablation. This lithospheric loss event was associated with
1028 upwelling return flow triggering decompression melting and magmatic activity at the surface.
1029 After this Late Jurassic episode, we envision two possibilities to explain the Eocene volcanics. The
1030 first is that there was a second episode of lithospheric instability and loss during the Eocene,
1031 possibly seeded by the emplacement of particularly dense material in the lithosphere during the
1032 Late Jurassic or aided by temporal changes in the density structure of the deep crust and/or the
1033 mantle lithosphere. A second possibility is that after the Late Jurassic, the thinned lithosphere was
1034 maintained via shear-driven upwelling until the present day, and there was an episode during the
1035 Eocene that involved either enhanced melt production or processes in the crust, perhaps involving
1036 a reorganization of the regional stress field, that allowed melt to reach the surface. Specifically, a
1037 change in plate motion may have enabled a pulse of particularly intense upwelling in the
1038 lithospheric divot during the Eocene, producing unusually large volumes of partial melt.
1039 Alternatively, a change in plate motion may have coincided with a reorganization of crustal
1040 stresses, allowing for partial melt that was already present in the uppermost mantle to find its way
1041 to the surface. In either case, we suggest that the most likely scenario since the Eocene is that the
1042 CAA lithospheric divot, whether it was created in its current form during the Late Jurassic or
1043 during the Eocene, has been maintained through small-scale mantle flow and shear-driven
1044 upwelling as the North American plate has continued to move over the underlying upper mantle.

1045 While the scenarios shown in Figure 8 generally match the observations summarized in
1046 this paper, and seem to be geodynamically plausible (e.g., Conrad & Molnar, 1997; Conrad et al.,
1047 2010, 2011), there are still some aspects of the observations that are not well explained. The origin
1048 and implications of a conductivity anomaly in the deep upper mantle documented by Evans et al.
1049 (2019) remain obscure. It is difficult to explain the lack of a present-day heat flow anomaly, and

1050 the presence of normal (as opposed to slow) crustal velocities above the thin lithosphere, if the
1051 lithospheric divot has been maintained over 50 Myr or more of geologic time. Furthermore, the
1052 controls on the timing of the second (Eocene) magmatic pulse remain poorly understood; whether
1053 triggered by a second episode of lithospheric foundering or by an intense pulse of shear-driven
1054 upwelling, we do not have a good understanding of what might have controlled the timing of the
1055 second event.

1056 Two non-exclusive possibilities can explain the apparent occurrence of a “headless”
1057 melting column (that is, the presence of partial melt in the uppermost mantle today with a lack of
1058 contemporaneous volcanism). First, present-day melt fractions could be too low beneath the
1059 remnant lithosphere to produce an eruption. Experimental constraints on the combined effects of
1060 melt-generation, the *in-situ* melt, and volatiles (Gaillard et al., 2008; Takei, 2017; Sifré et al., 2014;
1061 Yamauchi & Takei, 2016; Yoshino et al., 2010) suggest that geophysical anomalies could be
1062 explained by small, perhaps infinitesimal, melt fractions. Second, the remnant continental
1063 lithosphere and cold crust above the CAA may be essentially impermeable, such that any partial
1064 melt present in the shallow asthenosphere today cannot make its way to the surface. Under either
1065 condition, this portion of the passive margin of North America hosts a supra-solidus uppermost
1066 mantle with no present-day volcanic activity, and therefore represents a fascinating case study to
1067 understand the behavior of partial melt in the asthenosphere.

1068

1069 **8. Discussion and conclusions**

1070 *8.1 Unanswered questions and avenues for future work*

1071 A major outstanding question regarding the lithospheric loss event(s) beneath the Central
1072 Appalachians is to what extent the lower crust was involved, and whether the crustal density

1073 structure is important in driving lithospheric loss. As discussed above, there are some indications
1074 that the lower crust above the CAA today is denser than typical continental crust. One argument
1075 for excess density today comes from the particularly deep Moho beneath the mountains (Long et
1076 al., 2019), which may be explained by time-progressive metamorphic reactions in the roots of old
1077 mountain belts (Fischer, 2002). There are also observations of garnet-rich lower crustal xenoliths
1078 in Late Jurassic magmatic rocks above the CAA (Johnson et al., 2013), although it is not clear to
1079 what extent this observation might inform our view of lower crustal density either today or during
1080 the Eocene lithospheric loss event. One possible scenario is that particularly dense material was
1081 emplaced in the lower portion of the crust during the Late Jurassic and Eocene magmatic events.
1082 The emplacement of particularly dense (and seismically fast) material in the lower crust associated
1083 with volcanism at the surface has been inferred elsewhere in eastern North America, specifically
1084 in Mesozoic rift basins that host CAMP volcanics; examples include the South Georgia Basin
1085 (Marzen et al., 2020) and the Hartford Basin (Gao et al., 2020). Regardless of the source of the
1086 high-density material, the question of whether, and to what extent, the density structure of the
1087 lower crust plays a role in controlling lithospheric loss events is an important one. Some modeling
1088 work on catastrophic lithospheric loss has demonstrated that the lower crust, in addition to the
1089 lithospheric mantle, can be removed, and excess density in the lower crust can act as a driver for
1090 Rayleigh-Taylor instabilities (e.g., Krystopowicz & Currie, 2013). In other models of lithospheric
1091 instabilities, however, only the lower portion of the mantle lithosphere is involved (e.g., Conrad &
1092 Molnar, 1997). Future modeling work that is specific to the Central Appalachians and that
1093 considers a full suite of possible lithospheric density and rheology structure may help us to
1094 understand whether the lower crust was likely involved in past lithospheric loss event(s) and may

1095 make specific and testable predictions about the kind of lithospheric structures that should be
1096 expected today.

1097 A key outstanding question, and a compelling target for future work, is to understand
1098 whether the observations that are not obviously consistent with the preferred model presented in
1099 Section 7.2 can in fact be reconciled with it. Our preferred scenario (Figure 8) makes a few
1100 predictions that are not particularly consistent with the data. First, it remains somewhat unclear
1101 why there is no obvious, pronounced gravity anomaly associated with the CAA (Figure 5), if the
1102 CAA is indeed associated with the removal of dense continental lithosphere and its replacement
1103 with (perhaps continuously upwelling) less dense asthenospheric upper mantle. This question can
1104 likely be resolved in the future with detailed gravity modeling that takes into account the fine-scale
1105 details of crustal structure that have been resolved using MAGIC data. Second, if the lithosphere
1106 in the CAA region is indeed thin, and small-scale mantle flow is continuously driving upwelling
1107 in the mantle “divot” that brings relatively hot asthenosphere into contact with the base of a thin
1108 lithosphere, then it is unclear why there is no clear signature of elevated heat flow in the region.
1109 Third, if shear-driven upwelling has persisted since (at least) the Eocene, then one might expect a
1110 thermal anomaly, and thus relatively low seismic velocities, in the crust above the CAA; however,
1111 none of the tomographic models show a clear crustal velocity anomaly (Figure 3). A fourth
1112 apparent paradox stems from the fact that we observe elevated erosion rates in the CAA region
1113 today (Figure 7), and we can infer that they have either persisted since a hypothesized Eocene
1114 lithospheric removal event, or (more likely) reflect ongoing processes (small-scale mantle flow
1115 and shear-driven upwelling) that have themselves persisted since at least the Eocene. Despite the
1116 relatively fast erosion rates in the CAA region, however, we do not observe relatively thin crust,
1117 as one might expect from a prolonged period of fast erosion and associated isostatic adjustment.

1118 Another unsolved problem that represents a compelling target for future work is the
1119 question of how general the processes of lithospheric loss and evolution that we propose for the
1120 Central Appalachians might be. Is this set of processes specific to the Central Appalachians, or
1121 might they operate more broadly beneath passive continental margins, and thus play an important
1122 role in the evolution of continental lithosphere in a passive margin setting? If the former, then what
1123 are the aspects of the structure and evolution of the Central Appalachians that have led to its
1124 unusual lithospheric modification? If the latter, then can we see evidence for similar lithospheric
1125 evolution, either ongoing or in the recent past, in passive margin settings, and what does it imply
1126 for our understanding of how continental lithosphere evolves more generally?

1127

1128 *8.2 Summary*

1129 There are several independent lines of evidence for lithospheric loss beneath the Central
1130 Appalachian Mountains in the geologic past. The lithosphere associated with the CAA today is
1131 thin (likely < 80 km thick), as evidenced by geophysical anomalies in the upper mantle, including
1132 slow seismic velocities, high seismic attenuation, and high electrical conductivity. Receiver
1133 function imaging of the lithosphere-asthenosphere boundary is also consistent with a thin
1134 lithosphere beneath the Central Appalachians. These geophysical anomalies are co-located with a
1135 region of particularly high erosion rates; these may be linked directly to the lithospheric loss
1136 event(s), and/or may result from ongoing processes that maintain the thin lithosphere, such as
1137 shear-driven upwelling. There are two distinct episodes of intraplate magmatic activity that post-
1138 date the last major tectonic event (the breakup of Pangea), with one pulse of magmatism during
1139 the Late Jurassic and one during the Eocene. Geochemical and petrological investigation of the
1140 Late Jurassic and Eocene magmatic products provide constraints on the conditions of melting. We

1141 have articulated and evaluated a suite of conceptual models for lithospheric loss beneath the
1142 Central Appalachians and find support for a class of models that invoke either episodic lithospheric
1143 loss via Rayleigh-Taylor instabilities, or a Rayleigh-Taylor instability followed by small-scale
1144 convection and an episode of enhanced mantle upwelling driven by shearing. The thin lithosphere
1145 beneath the Central Appalachians has likely been maintained since the last episode of magmatic
1146 activity through processes that include small-scale mantle flow and/or shear-driven upwelling.
1147 While the exact mechanisms for lithospheric loss and intraplate volcanism beneath the Central
1148 Appalachians remain imperfectly understood, our synthesis has laid out what aspects of the
1149 present-day structure and the geochemical and petrological characteristics of the magmatic
1150 products are well understood, and what aspects still need to be studied. We have articulated several
1151 avenues for future work that may help to discriminate among the plausible models for the evolution
1152 of the Central Appalachian lithosphere. In particular, future modeling studies that seek to evaluate
1153 the conceptual models we propose here in a quantitative and regionally specific framework will
1154 help to evaluate their plausibility and consistency with observations in detail.

1155

1156 **Acknowledgements**

1157 This work benefited from discussions at the EarthScope Synthesis Workshop on the
1158 Evolution of the Southern Appalachian Lithosphere, held at Brown University in March 2017. We
1159 acknowledge support from the U.S. National Science Foundation via grants EAR-1460257 (RLE),
1160 EAR-1249412 (EG), EAR-1249438 (EAJ), EAR-1250988 (SDK), EAR-1251538 (EK), and EAR-
1161 1251515 (MDL). We thank Randy Keller for making the PACES gravity data available. The
1162 collection and dissemination of most of the geophysical data and models discussed in this paper
1163 were facilitated by the Incorporated Research Institutions for Seismology (IRIS). The facilities of

1164 the IRIS Consortium are supported by the U.S. National Science Foundation under Cooperative
1165 Agreement EAR-1261681.

1166

1167 **Data Availability Statement**

1168 No new data were generated as part of this study. Data from previously published sources that
1169 were used in this work are available through Duxbury et al. (2015), Long et al. (2020), Mazza et
1170 al. (2014, 2017), Perry et al. (1979), Portenga and Bierman (2011), and Portenga et al. (2019).
1171 Seismic and magnetotelluric data that underpin the geophysical models are available through the
1172 IRIS Data Management Center (<https://ds.iris.edu/ds/nodes/dmc/>). Many of the tomographic
1173 models are available through the IRIS Earth Model Collaboration
1174 (<http://ds.iris.edu/ds/products/emc/>).

1175

1176 **References**

1177

- 1178 Abers, G.A., Fischer, K.M., Hirth, G., Wiens, D.A., Plank, T., Holtzman, B.K., et al. (2014).
1179 Reconciling mantle attenuation-temperature relationships from seismology, petrology, and
1180 laboratory measurements. *Geochemistry, Geophysics, Geosystems*, *15*, 3521–3542.
1181 <https://doi.org/10.1002/2014GC005444>.
- 1182 Aragon, J. C., Long, M. D., & Benoit, M. H. (2017). Lateral variations in SKS splitting across the
1183 MAGIC array, central Appalachians. *Geochemistry, Geophysics, Geosystems*, *18*, 4136–4155.
1184 <https://doi.org/10.1002/2017GC007169>.
- 1185 Bailey, D. G., & Lupulescu, M.V. (2015). Spatial, temporal, mineralogical, and compositional
1186 variations in Mesozoic kimberlitic magmatism in New York State. *Lithos*, *212*, 298–310.
1187 <https://doi.org/10.1016/j.lithos.2014.11.022>
- 1188 Baba, K., Chave, A. D., Evans, R. L., Hirth, G., & Mackie, R. L. (2006a). Mantle dynamics beneath
1189 the East Pacific Rise at 17°S: Insights from the Mantle Electromagnetic and Tomography
1190 (MELT) experiment. *Journal of Geophysical Research: Solid Earth*, *111*(B2), B02101.
1191 <https://doi.org/10.1029/2004JB003598>.
- 1192 Baba, K., Tarits, P., Chave, A. D., Evans, R. L., Hirth, G., & Mackie, R. L. (2006b). Electrical
1193 structure beneath the northern MELT line on the East Pacific Rise at 15°45'S. *Geophysical
1194 Research Letters*, *33*, L22301. <https://doi.org/10.1029/2006GL027528>.
- 1195 Babikoff, J.C., & Dalton, C.A. (2019). Long-period Rayleigh wave phase velocity tomography
1196 using USArray. *Geochemistry, Geophysics, Geosystems*, *20*(4), 1990–2006.
1197 <https://doi.org/10.1029/2018GC008073>.

1198 Ballmer, M. D., Conrad, C. P., Smith, E. I., & Johnsen, R. (2015). Intraplate volcanism at the edges
1199 of the Colorado Plateau sustained by a combination of triggered edge-driven convection and
1200 shear-driven upwelling. *Geochemistry, Geophysics, Geosystems*, *16*, 366-379. [https://doi.org/](https://doi.org/10.1002/2014GC005641)
1201 [10.1002/2014GC005641](https://doi.org/10.1002/2014GC005641).

1202 Baldwin, J. A., Whipple, K. X., & Tucker, G. E. (2003). Implications of the shear stress river
1203 incision model for the timescale of postorogenic decay of topography. *Journal of Geophysical*
1204 *Research: Solid Earth*, *108*(B3), 2158. <https://doi.org/10.1029/2001JB000550>.

1205 Benoit, M. H., Long, M. D., & King, S. D. (2013). Anomalously thin transition zone and apparently
1206 isotropic upper mantle beneath Bermuda: Evidence for upwelling. *Geochemistry, Geophysics,*
1207 *Geosystems*, *14*, 4282-4291. <https://doi.org/10.1002/ggge.20277>.

1208 Bensen, G.D., Ritzwoller, M.H., & Shapiro, N.M. (2008). Broadband ambient noise surface wave
1209 tomography across the United States. *Journal of Geophysical Research: Solid Earth*, *113*,
1210 B05306. <https://doi.org/10.1029/2007JB005248>.

1211 Bezada, M.J. (2017). Insights into the lithospheric architecture of Iberia and Morocco from
1212 teleseismic body-wave attenuation. *Earth and Planetary Science Letters*, *478*, 14–26.
1213 <https://doi.org/10.1016/j.epsl.2017.08.029>.

1214 Bezada, M.J., Byrnes, J., & Eilon, Z. (2019). On the robustness of attenuation measurements on
1215 teleseismic P waves: insights from micro-array analysis of the 2017 North Korean nuclear test.
1216 *Geophysical Journal International*, *218*, 573 – 585. <https://doi.org/10.1093/gji/ggz169>.

1217 Bikerman, M., Prellwitz, H. S., Dembosky, J., Simonetti, A., & Bell, K. (1997). New phlogopite
1218 K-Ar dates and the age of southwestern Pennsylvania kimberlite dikes. *Northeastern Geology*
1219 *and Environmental Sciences*, *19*, 302-308.

1220 Bina, C. R., & Helffrich, G. (1994). Phase transition Clapeyron slopes and transition zone
1221 seismic discontinuity topography. *Journal of Geophysical Research: Solid Earth*, *99*, 15,853
1222 – 15,860. <https://doi.org/10.1029/94JB00462>.

1223 Birch, F. (1961). The velocity of compressional waves in rocks to 10 kilobars, Part 2. *Journal of*
1224 *Geophysical Research: Solid Earth*, *66*, 2199-2224. [https://doi.org/10.1029/](https://doi.org/10.1029/JZ066i007p02199)
1225 [JZ066i007p02199](https://doi.org/10.1029/JZ066i007p02199).

1226 Biryol, C. B., Wagner, L. S., Fischer, K. M., & Hawman, R.B. (2016). Relationship between
1227 observed upper mantle structures and recent tectonic activity across the Southeastern United
1228 States. *Journal of Geophysical Research: Solid Earth*, *121*(5), 3393-3414.
1229 <https://doi.org/10.1022/2015JB012698>.

1230 Blackburn, T. J., Olsen, P. E., Bowring, S. A., McLean, N. M., Kent, D. V., Puffer, J., McHone,
1231 G., Rasbury, E. T., & Et-Touhami, M. (2013). Zircon U-Pb geochronology links the end-
1232 Triassic extinction with the Central Atlantic Magmatic Province. *Science*, *340*, 941-945.
1233 <https://doi.org/10.1126/science.1234204>.

1234 Blackman, D. K., & Kendall, J.-M. (2002). Seismic anisotropy in the upper mantle: 2. Predictions
1235 for current plate boundary flow models. *Geochemistry, Geophysics, Geosystems*, *3*, 1-26.
1236 <https://doi.org/10.1029/2001GC000247>.

1237 Boyce, A., Bastow, I. D., Golos, E. M., Rondenay, S., Burdick, S., & Van der Hilst, R.D. (2019).
1238 Variable modification of continental lithosphere during the Proterozoic Grenville orogeny:
1239 Evidence from teleseismic P-wave tomography. *Earth and Planetary Science Letters*, *525*,
1240 115763. <https://doi.org/10.1016/j.epsl.2019.115763>.

1241 Burton, W.C., & Southworth, S. (2010). A model for Iapetan rifting of Laurentia based on
1242 Neoproterozoic dikes and related rocks, *in* Tollo, R. P., Bartholomew, M. J., Hibbard, J. P., &

1243 Karabinos, P.M., eds., From Rodinia to Pangea: The Lithotectonic Record of the Appalachian
1244 Region, Geological Society of America, Boulder, CO, Memoir 206, pp. 455-476.

1245 Byrnes, J. S., Bezada, M., Long, M. D., & Benoit, M. H. (2019). Thin lithosphere beneath the
1246 central Appalachian Mountains: Constraints from seismic attenuation beneath the MAGIC
1247 array. *Earth and Planetary Science Letters*, 519, 297-307. [https://doi.org/10.1016/
1248 j.epsl.2019.04.045](https://doi.org/10.1016/j.epsl.2019.04.045).

1249 Callegaro, S., Marzoli, A., Bertrand, H., Chiaradia, M., Reisberg, L., Meyzen, C., et al. (2013).
1250 Upper and lower crust recycling in the source of CAMP basaltic dykes from southeastern North
1251 America. *Earth and Planetary Science Letters*, 376, 186–199. [https://doi.org/
1252 10.1016/j.epsl.2013.06.023](https://doi.org/10.1016/j.epsl.2013.06.023)

1253 Chu, R., Leng, W., Helmberger, D. V., & Gurnis, M. (2013). Hidden hotspot track beneath the
1254 eastern United States. *Nature Geoscience*, 6, 963-966. <https://doi.org/10.1038/NCEO1949>.

1255 Conrad, C. P., Wu, B., Smith, E. I., Bianco, T. A., & Tibbetts, A. (2010). Shear-driven upwelling
1256 induced by lateral viscosity variations and asthenospheric shear: A mechanism for intraplate
1257 volcanism. *Physics of the Earth and Planetary Interiors*, 178, 162-175.
1258 <https://doi.org/10.1016/j.pepi.2009.10.001>.

1259 Conrad, C. P., Bianco, T. A., Smith, E. I., & Wessel, P. (2011). Patterns of intraplate volcanism
1260 controlled by asthenospheric shear. *Nature Geoscience*, 4, 317-321.
1261 <https://doi.org/10.1038/ngeo1111>.

1262 Conrad, C. P., & Molnar, P. (1997). The growth of Rayleigh-Taylor-type instabilities in the
1263 lithosphere for various rheological and density structures. *Geophysical Journal International*,
1264 129, 95-112. <https://doi.org/10.1111/j.1365-246X.1997.tb00939.x>.

1265 Cook, F. A. (1984). Towards and understanding of the southern Appalachian Piedmont crustal
1266 transition – A multidisciplinary approach. *Tectonophysics*, 109, 77-92.
1267 [https://doi.org/10.1016/0040-1951\(84\)90171-9](https://doi.org/10.1016/0040-1951(84)90171-9).

1268 Davis, W.M. (1889). The rivers and valleys of Pennsylvania. *National Geographic Magazine* 1,
1269 183-253.

1270 DiBiase, R.A., Denn, A.R., Bierman, P.R., Kirby, E., West, N., & Hidy, A.J. (2018). Stratigraphic
1271 control of landscape response to base-level fall, Young Womans Creek, Pennsylvania, USA.
1272 *Earth and Planetary Science Letters*, 504, 263-173, [https://doi.org/10.1016/
1273 j.epsl.2018.10.005](https://doi.org/10.1016/j.epsl.2018.10.005).

1274 DiBiase, R.A., & Whipple, K.X. (2011). The influence of erosion thresholds and runoff variability
1275 on the relationships among topography, climate, and erosion rate. *Journal of Geophysical
1276 Research: Earth Surface*, 116, F04036. <https://doi.org/10.1029/2011JF002095>.

1277 DiBiase, R.A., Whipple, K.X., Heimsath, A.M., & Ouimet, W.B. (2010). Landscape form and
1278 millennial erosion rates in the San Gabriel Mountains, CA. *Earth and Planetary Science
1279 Letters*, 289, 134-144. <https://doi.org/10.1016/j.epsl.2009/10.036>.

1280 Dicken, C. L., Nicholson, S. W., Horton, J.D., Kinney, S. A., Gunther, G., Foose, M. P., &
1281 Mueller, J. A. L. (2005). Preliminary integrated geologic map databases for the United States:
1282 Delaware, Maryland, New York, Pennsylvania, and Virginia. U.S. Geological Survey Open
1283 File Report 2005-1325, accessed January 31, 2013, at <https://pubs.usgs.gov/of/2005/1325>.

1284 Dong, M. T., & Menke, W. H. (2017). Seismic high attenuation region observed beneath southern
1285 New England from teleseismic body wave spectra: Evidence for high asthenospheric
1286 temperature without melt. *Geophysical Research Letters*, 44, 10,958-10,969.
1287 <https://doi.org/10.1002/2017GL074953>.

1288 Duxbury, J., Bierman, P. R., Portenga, E. W., Pavich, M. J., Southworth, S., & Freeman, S. P.
1289 (2015). Erosion rates in and around Shenandoah National Park, Virginia, determined using
1290 analysis of cosmogenic ^{10}Be . *American Journal of Science*, 315, 46-76. [https://doi.org/](https://doi.org/10.2475/01.2015.02)
1291 [10.2475/01.2015.02](https://doi.org/10.2475/01.2015.02).

1292 Dziewonski, A.M. & Anderson, D.L. (1981). Preliminary Reference Earth Model. *Physics of the*
1293 *Earth and Planetary Interiors*, 25(4), 297-356. [https://doi.org/10.1016/0031-9201\(81\)90046-](https://doi.org/10.1016/0031-9201(81)90046-7)
1294 [7](https://doi.org/10.1016/0031-9201(81)90046-7).

1295 Eilon, Z. C., & Abers, G. A. (2017). High seismic attenuation at a mid-ocean ridge reveals the
1296 distribution of deep melt. *Science Advances*, 3(5), e1602829. [https://doi.org/10.126/](https://doi.org/10.126/sciadv.1602829)
1297 [sciadv.1602829](https://doi.org/10.126/sciadv.1602829).

1298 Elkins-Tanton, L. T. (2007). Continental magmatism, volatile recycling, and a heterogeneous
1299 mantle caused by lithospheric gravitational instabilities. *Journal of Geophysical Research:*
1300 *Solid Earth*, 112, B03405. <https://doi.org/10.1029/2005JB004072>.

1301 Evans, R. R., Benoit, M. H., Long, M. D., Elsenbeck, J., Ford, H. A., Zhu, J., & Garcia, X. (2019).
1302 Thin lithosphere beneath the central Appalachian Mountains: A combined seismic and
1303 magnetotelluric study. *Earth and Planetary Science Letters*, 519, 308-316.
1304 <https://doi.org/10.1016/j.epsl.2019.04.46>.

1305 Fernandes, V. M., Roberts, G. G., White, N., & Whittaker, A. C. (2019). Continental-scale
1306 landscape evolution: A history of North American topography. *Journal of Geophysical*
1307 *Research: Earth Surface*, 124(11), 2689-2722. <https://doi.org/10.1029/2018JF004979>.

1308 Fischer, K.M. (2002). Waning buoyancy in the crustal roots of old mountains. *Nature*, 417, 933–
1309 936. <https://doi.org/10.1038/nature00855>.

1310 Foland, K., Gilbert, L. A., Sebring, C. A., & Jiang-Feng, C. (1986). $^{40}\text{Ar}/^{39}\text{Ar}$ ages for plutons of
1311 the Montereian Hills, Quebec: Evidence for a single episode of Cretaceous magmatism.
1312 *Geological Society of America Bulletin*, 97(8), 966–974. [https://doi.org/10.1130/0016-](https://doi.org/10.1130/0016-7606(1986)97)
1313 [7606\(1986\)97](https://doi.org/10.1130/0016-7606(1986)97).

1314 Foland, K. A., Quinn, A. W., & Giletti, B. J. (1971). K-Ar and Rb-Sr Jurassic and Cretaceous ages
1315 for intrusives of the White Mountain magma series, northern New England. *American Journal*
1316 *of Science*, 270(5), 321-330. <https://doi.org/10.2475/ajs.270.5.321>.

1317 Frone, Z. S., Blackwell, D. D., Richards, M. C., & Hornbach, M. J. (2015). Heat flow and thermal
1318 modeling of the Appalachian Basin, West Virginia. *Geosphere*, 11(5), 1279-1290.
1319 <https://doi.org/10.1130/GES01155.1>.

1320 Gaillard, F., Malki, M., Iacono-Marziano, G., Pichavant, M., & Scaillet, B. (2008). Carbonatite
1321 melts and electrical conductivity in the asthenosphere. *Science*, 322, 1363-1365.
1322 <https://doi.org/10.1126/science.1164446>.

1323 Gallen, S.F. (2018). Lithologic controls on landscape dynamics and aquatic species evolution in
1324 post-orogenic mountains. *Earth and Planetary Science Letters*, 493, pp.150-160.
1325 <https://doi.org/10.1016/j.epsl/2018.04.029>.

1326 Gallen, S. F., Wegmann, K. W., & Bohnenstiehl, D. R. (2013). Miocene rejuvenation of
1327 topographic relief in the southern Appalachians. *GSA Today*, 23, 4-10.
1328 <https://doi.org/10.1130/GSATG163A.1>.

1329 Gao, S. S., & Liu, K. H. (2014). Mantle transition zone discontinuities beneath the contiguous
1330 United States. *Journal of Geophysical Research: Solid Earth*, 119, 6452-6468.
1331 <https://doi.org/10.1002.2014JB011253>.

- 1332 Gao, H., Yang, X., Long, M. D., & Aragon, J. C. (2020). Seismic evidence for crustal modification
1333 beneath the Hartford Rift Basin in the Northeastern United States. *Geophysical Research*
1334 *Letters*, 47, e2020GL089316. <https://doi.org/10.1029/2020GL089316>.
- 1335 Golos, E.M., Fang, H., Yao, H., Zhang, H., Burdick, S., Vernon, F., et al. (2018). Shear wave
1336 tomography beneath the United States using a joint inversion of surface and body waves.
1337 *Journal of Geophysical Research: Solid Earth*, 123(6), 5169-5189. [https://doi.org/](https://doi.org/10.1029/2017JB014894)
1338 [10.1029/2017JB014894](https://doi.org/10.1029/2017JB014894).
- 1339 Goren, L., Fox, M., & Willett, S.D. (2014). Tectonics from fluvial topography using formal linear
1340 inversion: Theory and applications to the Inyo Mountains, California. *Journal of Geophysical*
1341 *Research: Earth Surface*, 119, 1651-1681. <https://doi.org/10.1002/2014JF003079>.
- 1342 Gripp, A. E., & Gordon, R. G. (2002). Young tracks of hotspots and current plate velocities.
1343 *Geophysical Journal International*, 150(2), 321-361. [https://doi.org/10.1046/j.1365-](https://doi.org/10.1046/j.1365-246X.2002.01627.x)
1344 [246X.2002.01627.x](https://doi.org/10.1046/j.1365-246X.2002.01627.x).
- 1345 Griscom, A. (1963). Tectonic significance of the Bouguer gravity field of the Appalachian System.
1346 *Geological Society of America Special Paper*, 73, 163-164.
- 1347 Hack, J. T. (1960). Interpretation of erosional topography in humid temperate regions. *American*
1348 *Journal of Science*, 258, pp.80–97.
- 1349 Hancock, G., & Kirwan, M. (2007). Summit erosion rates deduced from ¹⁰Be; implications for
1350 relief production in the Central Appalachians. *Geology*, 35, 89–92. [https://doi.org/10.1130/](https://doi.org/10.1130/G23147A.1)
1351 [G23147A.1](https://doi.org/10.1130/G23147A.1).
- 1352 Harkins, N., Kirby, E., Heimsath, A., Robinson, R., & Reiser, U. (2007). Transient fluvial incision
1353 in the headwaters of the Yellow River, northeastern Tibet, China. *Journal of Geophysical*
1354 *Research: Earth Surface*, 112, F03S04. <https://doi.org/10.1029/2006JF000570>.
- 1355 Hatcher, Jr., R.D. (2010). The Appalachian orogeny: A brief summary, in Tollo, R. P.,
1356 Bartholomew, M. J., Hibbard, J. P., & Karabinos, P. M., eds., From Rodinia to Pangea: The
1357 Lithotectonic Record of the Appalachian Region, Geological Society of America, Boulder,
1358 CO, Memoir 206, pp. 1-19.
- 1359 Havlin, C., Parmentier, E. M., & Hirth, G (2013). Dike propagation driven by melt accumulation
1360 at the lithosphere–asthenosphere boundary. *Earth and Planetary Science Letters*, 376, 20-
1361 28. <https://doi.org/10.1016/j.epsl.2013.06.010>.
- 1362 Haynes, J. T., Johnson, E. A., & Whitmeyer, S. J. (2014). Active features along a “passive” margin:
1363 The intriguing interplay between Silurian-Devonian stratigraphy, Alleghanian deformation,
1364 and Eocene magmatism of Highland and Bath Counties, Virginia, in Bailey, C. M., & Coiner,
1365 L.V., eds., Elevating Geoscience in the Southeastern United States: New Ideas about Old
1366 Terranes: Field Guides for the GSA Southeastern Section Meeting, Blacksburg, Virginia, 2014.
1367 Geological Society of America Field Guide 35, 1-40, [https://doi.org/10.1130/2014.0035\(01\)](https://doi.org/10.1130/2014.0035(01)).
- 1368 Hibbard, J. P., van Staal, C. R., & Rankin, D. W. (2010). Comparative analysis of the geological
1369 evolution of the northern and southern Appalachian orogeny: Late Ordovician-Permian, in
1370 Tollo, R. P., Bartholomew, M. J., Hibbard, J. P., & Karabinos, P. M., eds., From Rodinia to
1371 Pangea: The Lithotectonic Record of the Appalachian Region, Geological Society of America,
1372 Boulder, CO, Memoir 206, pp. 51-69.
- 1373 Hutchinson, D. R., Klitgord, K. D., & Detrick, R. S. (1986). Rift basins of the Long Island
1374 platform. *Geological Society of America Bulletin*, 97, 688-702. [https://doi.org/10.1130/0016-](https://doi.org/10.1130/0016-7606(1986)97<688:RBOTLI>2.0.CO;2)
1375 [7606\(1986\)97<688:RBOTLI>2.0.CO;2](https://doi.org/10.1130/0016-7606(1986)97<688:RBOTLI>2.0.CO;2).
- 1376 Ito, G., Dunn, R., & Li, A. (2015). The origin of shear wave splitting beneath Iceland. *Geophysical*
1377 *Journal International*, 201, 1297-1312. <https://doi.org/10.1093/gji/ggv078>.

1378 Jacobsen, B. H. (1987). A case for upward continuation as a standard separation filter for potential-
1379 field maps. *Geophysics*, 52, 1033-1165. <https://doi.org/10.1190/1.1442378>.

1380 Johnson, R. W., Milton, C., & Dennison, J. M. (1971). Field trip to the igneous rocks of Augusta,
1381 Rockingham, Highland, and Bath counties, Virginia. *Virginia Division of Mineral Resources*,
1382 16, 1–68.

1383 Johnson, E. A., Kiracofe, Z. A., Haynes, J. T., & Nashimoto, K. (2013). The origin of sandstone
1384 xenoliths in the Mole Hill basalt, Rockingham County, Virginia: Implications for magma
1385 ascent and crustal structure in the western Shenandoah Valley. *Southeastern Geology*, 49, 95–
1386 118.

1387 Kaislaniemi, L., & van Hunen, J. (2014). Dynamics of lithospheric thinning and mantle melting
1388 by edge-driven convection: Application to Moroccan Atlas mountains. *Geochemistry*,
1389 *Geophysics, Geosystems*, 15, 3175-3189. <https://doi.org/10.1002/2014GC005414>.

1390 Karner, G. D., & Watts, A. B. (1983). Gravity anomalies and flexure of the lithosphere at mountain
1391 ranges. *Journal of Geophysical Research: Solid Earth*, 88(B12), 10449-10477. <https://doi.org/10.1029/JB088uB12p10449>.

1392

1393 Keifer, I., & Dueker, K. (2019). Testing the hypothesis that temperature modulates 410 and 660
1394 discontinuity topography beneath the eastern United States. *Earth and Planetary Science*
1395 *Letters*, 524, 115723. <https://doi.org/10.1016/j.epsl.2019.115723>.

1396 Kennett, B. L. N., & Engdahl, E. R. (1991). Traveltimes for global earthquake location and phase
1397 identification. *Geophysical Journal International*, 105, 429-465. [https://doi.org/10.1111/](https://doi.org/10.1111/j.13640246X.1991.tb06724.x)
1398 [j.13640246X.1991.tb06724.x](https://doi.org/10.1111/j.13640246X.1991.tb06724.x).

1399 Key, K., Constable, S., Liu, L., & Pommier, A. (2013). Electrical image of passive mantle
1400 upwelling beneath the northern East Pacific Rise. *Nature*, 495, 499-502.
1401 <https://doi.org/10.1038/nature11932>.

1402 King, S.D. (2007), Hotspots and edge-driven convection. *Geology*, 35, 223-226.
1403 <https://doi.org/10.1130/G23291A.1>.

1404 King, S. D., & Anderson, D. L. (1998). Edge-driven convection. *Earth and Planetary Science*
1405 *Letters*, 160, 289-296. [https://doi.org/10.1016/S0012-821X\(98\)00089-2](https://doi.org/10.1016/S0012-821X(98)00089-2).

1406 Kinney, S., Maclennan, S. A., Setera, J., Schoene, B., VanTongeren, J., Strauss, J. V., et al. (2020).
1407 Long-lived and localized post-orogenic magmatism on the eastern North American margin:
1408 insights from zircon U-PB geochronology. *Geological Society of America Abstracts with*
1409 *Programs*, 10.1130/abs/2020SE-345449.

1410 Kirby, E., & Whipple, K. X. (2012). Expression of active tectonics in erosional landscapes.
1411 *Journal of Structural Geology*, 44, 54-75. <https://doi.org/10.1016/j.jsg.2012.07.009>.

1412 Krystopowicz, N. J., & Currie, C. A. (2013). Crustal eclogitization and lithospheric delamination
1413 in orogens. *Earth and Planetary Science Letters*, 361, 195-207.
1414 <https://doi.org/10.1016/j.epsl.2012.09.056>.

1415 Lague, D. (2014). The stream power river incision model: evidence, theory and beyond. *Earth*
1416 *Surface Processes and Landforms*, 39, 38-61. <http://doi.org/10.1002/esp.3462>.

1417 Lekic, V., & Romanowicz, B. (2011). Tectonic regionalization without a priori information: A
1418 cluster analysis of upper mantle tomography. *Earth and Planetary Science Letters*, 308, 151–
1419 160. <https://doi.org/10.1016/j.epsl.2011.05.050>.

1420 Levandowski, W., Hermann, R. B., Briggs, R., Boyd, O., & Gold, R. (2018). An updated stress
1421 map of the continental United States reveals heterogeneous intraplate stress. *Nature*
1422 *Geoscience*, 11, 433-437. <https://doi.org/10.1038/s41561-018-0120-x>.

1423 Levin, V., Long, M. D., Skryzalin, P., Li, Y., & López, I. (2018). Seismic evidence for a recently
1424 formed mantle upwelling beneath New England. *Geology*, *46*, 87-90.
1425 <https://doi.org/10.1130/G39641.1>.

1426 Li, C., Gao, H., & Williams, M. L. (2020). Seismic characteristics of the eastern North American
1427 crust with Ps converted waves: Terrane accretion and modification of continental crust.
1428 *Journal of Geophysical Research: Solid Earth*, *125*, e2019JB018727. [https://doi.org/](https://doi.org/10.1029/2019JB018727)
1429 [10.1029/2019JB018727](https://doi.org/10.1029/2019JB018727).

1430 Li, Z. X., Bogdanova, S.V., Collins, A.S., Davison, A., De Waele, B., Ernst, R.E., et al. (2008).
1431 Assembly, configuration, and break-up history of Rodinia: A synthesis. *Precambrian*
1432 *Research*, *160*, 179-210. <https://doi.org/10.1016/j.precamres.2007.04.021>.

1433 Lin, F.-C., Ritzwoller, M. H., & Snieder, R. (2009). Eikonal tomography: Surface wave
1434 tomography by phase-front tracking across a regional broad-band seismic array. *Geophysical*
1435 *Journal International*, *177*, 1091–1110. <https://doi.org/10.1111/j.1365-246X.2009.04105.x>.

1436 Lin, F. C., & Ritzwoller, M. H. (2011). Helmholtz surface wave tomography for isotropic and
1437 azimuthally anisotropic structure. *Geophysical Journal International*, *186*, 1104–1120.
1438 <https://doi.org/10.1111/j.1365-246X.2011.05070.x>.

1439 Liu, L. (2014). Rejuvenation of Appalachian topography caused by subsidence-induced
1440 differential erosion. *Nature Geoscience*, *7*, 518-523. <https://doi.org/10.1038/NNGEO2187>.

1441 Liu, S., Aragon, J. C., Benoit, M. H., Long, M. D., & King, S. D. (2018). Transition zone structure
1442 beneath the eastern U.S. *AGU Fall Meeting*, Washington, DC, abstract T52D-05.

1443 Liu, Y., & Holt, W. E. (2015). Wave gradiometry and its link with Helmholtz equation solutions
1444 applied to USArray in the eastern US. *Journal of Geophysical Research: Solid Earth*, *120*,
1445 5717–5746. <https://doi.org/10.1002/2015JB011982>.

1446 Long, L. T. (1979). The Carolina slate belt – Evidence of a continental rift zone. *Geology*, *7*, 180-
1447 184. [https://doi.org/10.1130/0091-7613\(1979\)7<180:TCSBOA>2.0.CO;2](https://doi.org/10.1130/0091-7613(1979)7<180:TCSBOA>2.0.CO;2).

1448 Long, M. D., Benoit, M. H., Chapman, M. C., & King, S. D. (2010). Upper mantle anisotropy and
1449 transition zone thickness beneath southeastern North America and implications for mantle
1450 dynamics. *Geochemistry, Geophysics, Geosystems*, *11*, Q10012. [https://doi.org/10.1029/](https://doi.org/10.1029/2010GC003247)
1451 [2010GC003247](https://doi.org/10.1029/2010GC003247).

1452 Long, M. D., Jackson, K. G., & McNamara, J. F. (2016). SKS splitting beneath Transportable
1453 Array stations in eastern North America and the signature of past lithospheric deformation.
1454 *Geochemistry, Geophysics, Geosystems*, *17*, 2-15. <https://doi.org/10.1029/2015GC006088>.

1455 Long, M. D., Benoit, M. H., Aragon, J. C., & King, S. D. (2019). Seismic imaging of mid-crustal
1456 structure beneath central and eastern North America: Possibly the elusive Grenville
1457 deformation? *Geology*, *47*, 371-374. <https://doi.org/10.1130/G46077.1>.

1458 Long, M. D., Benoit, M. H., Evans, R. L., Aragon, J. C., & Elsenbeck, J. (2020). The MAGIC
1459 experiment: A combined seismic and magnetotelluric deployment to investigate the structure,
1460 dynamics, and evolution of the central Appalachians. *Seismological Research Letters*, *91*,
1461 2960-2975. <https://doi.org/10.1785/0220200150>.

1462 Magni, V., & Király, Á. (2020). Delamination. *Reference Module in Earth Systems and*
1463 *Environmental Sciences*, Elsevier. <https://doi.org/10.1016/B978-0-12-409548-9.09515-4>.

1464 Marzen, R. E., Shillington, D. J., Lizarralde, D., Knapp, J. H., Heffner, D. M., Davis, J. K., &
1465 Harder, S. H. (2020). Limited and localized magmatism in the Central Atlantic Magmatic
1466 Province. *Nature Communications*, *11*, 3397. <https://doi.org/10.1038/s41467-020-17193-6>.

1467 Marzoli, A., Callegaro, S., Dal Corso, J., Davies, J. H. F. L., Chiaradia, M., Youbi, N., et al. (2018).
1468 The Central Atlantic Magmatic Province (CAMP): A review. In: Tanner, L. H., ed., *The Late*
1469 *Triassic World, Topics in Geobiology*, vol. 46, pp. 91-125. New York, NY: Springer.

1470 Matmon, A., Bierman, P. R., Larsen, J., Southworth, S., Pavich, M. J., & Caffee, M. W. (2003).
1471 Temporally and spatially uniform rates of erosion in the southern Appalachian Great Smoky
1472 Mountains. *Geology*, *31*, 155-158. [https://doi.org/10.1130/0091-7613\(2003\)031](https://doi.org/10.1130/0091-7613(2003)031)
1473 <0155:TASURO>2.0.CO;2.

1474 Mazza, S. E., Gazel, E. A., Johnson, E. A., Bizimis, M., McAleer, R., & Biryol, C. B. (2017). Post-
1475 rift magmatic evolution of the eastern North American “passive-aggressive” margin.
1476 *Geochemistry, Geophysics, Geosystems*, *18*, 3-22, <https://doi.org/10.1002/2016GC006646>.

1477 Mazza, S. E., Gazel, E., Johnson, E. A., Kunk, M. J., McAleer, R., Spotila, J. A., Bizimis, M., &
1478 Coleman, D. S. (2014). Volcanoes of the passive margin: The youngest magmatic event in
1479 eastern North America. *Geology*, *42*, 483-486. <https://doi.org/10.1130/G35407.1>.

1480 McHone, J. G. (1996), Constraints on the mantle plume model for Mesozoic alkaline intrusions in
1481 northeastern North America. *Canadian Mineralogist*, *34*, 325–334.

1482 McLelland, J. M., Selleck, M. W., & Bickford, M. E. (2010). Review of the Proterozoic evolution
1483 of the Grenville Province, its Adirondack outlier, and the Mesoproterozoic inliers of the
1484 Appalachians, in Tollo, R.P., Bartholomew, M. J., Hibbard, J. P., & Karabinos, P. M., eds.,
1485 From Rodinia to Pangea: The Lithotectonic Record of the Appalachian Region, Geological
1486 Society of America, Boulder, CO, Memoir 206, pp. 21-49.

1487 Menke, W., Skryzalin, P., Levin, V., Harper, T., Darbyshire, F., & Dong, T. (2016). The Northern
1488 Appalachian Anomaly: A modern asthenospheric upwelling. *Geophysical Research Letters*,
1489 *43*, 10,173-10,179, <https://doi.org/10.1002/2016GL070918>.

1490 Menke, W., Lamoureux, J., Abbott, D., Hopper, E., Hutson, D., & Marrero, A. (2018). Crustal
1491 heating and lithospheric alteration and erosion associated with asthenospheric upwelling
1492 beneath southern New England (USA). *Journal of Geophysical Research: Solid*
1493 *Earth*, *123*(10), 8995-9008. <https://doi.org/10.1029/2018JB015921>.

1494 Miller, S. R., Sak, P. B., Kirby, E., & Bierman, P. R. (2013). Neogene rejuvenation of central
1495 Appalachian topography: Evidence for differential rock uplift from stream profiles and erosion
1496 rates. *Earth and Planetary Science Letters*, *369*, 1-12. [https://doi.org/10.1016/](https://doi.org/10.1016/j.epsl.2013.04.007)
1497 [j.epsl.2013.04.007](https://doi.org/10.1016/j.epsl.2013.04.007).

1498 Moucha, R., Forte, A. M., Mitrovica, J. X., Rowley, D. B., Quéré, S., Simmons, N. A., & Grand,
1499 S.P. (2008). Dynamic topography and long-term sea-level variations: There is no such thing as
1500 a stable continental platform. *Earth and Planetary Science Letters*, *271*, 101-108.
1501 <https://doi.org/10.1016/j.epsl.2008.03.056>.

1502 Moucha, R., & Ruetenik, G. A. (2017). Interplay between dynamic topography and flexure along
1503 the US Atlantic passive margin: Insights from landscape evolution modeling. *Global and*
1504 *Planetary Change*, *149*, 72-78. <https://doi.org/10.1016/j.gloplacha.2017.01.004>.

1505 Naeser, C. W., Naeser, N. D., Newell, W. L., Southworth, S., Edwards, L.E., & Weems, R.E.
1506 (2016). Erosional and depositional history of the Atlantic passive margin as recorded in detrital
1507 zircon fission-track ages and lithic detritus in Atlantic Coastal Plain sediments. *American*
1508 *Journal of Science*, *316*, 110-160. <https://doi.org/10.2475/02.2016.02>.

1509 Nicholson, S. W. D., Horton, C. L., Labay, J. D., Foose, K. A., Mueller, M. P., & Julia, A. L.
1510 (2005). Preliminary integrated geologic map databases for the United States: Kentucky, Ohio,
1511 Tennessee, and West Virginia: U.S. Geological Survey Open File Report 2005-1324, accessed
1512 January 31, 2013, at <https://pubs.usgs.gov/of/2005/1324>.

1513 Pazzaglia, F. J., & Brandon, M. T. (1996). Macrogeomorphic evolution of the post-Triassic
1514 Appalachian mountains determined by deconvolution of the offshore basin sedimentary
1515 record. *Basin Research*, 8, 255-278. <https://doi.org/10.1046/j.1365-2117.1996.00274.x>.

1516 Perron, J. T., & Royden, L. (2013). An integral approach to bedrock river profile analysis. *Earth*
1517 *Surface Processes and Landforms*, 38(6), 570-576. <https://doi.org/10.1002/esp.3302>.

1518 Perry, L. D., Costain, J. K., & Geiser, P. A. (1979). Heat flow in western Virginia and a model for
1519 the origin of thermal springs in the folded Appalachians. *Journal of Geophysical Research:*
1520 *Solid Earth*, 84(B12), 6875-6883. <https://doi.org/10.1029/JB084iB12p06875>.

1521 Pollitz, F. F., & J. A. Snoke (2010). Rayleigh-wave phase-velocity maps and three-dimensional
1522 shear-velocity structure of the western US from local non-plane surface-wave tomography.
1523 *Geophysical Journal International*, 180, 1153–1169. [https://doi.org/10.1111.j.1365-246X.2009.04441.x](https://doi.org/10.1111/j.1365-246X.2009.04441.x).

1525 Pollitz, F.F., & Mooney, W.D. (2016). Seismic velocity structure of the crust and shallow mantle
1526 of the Central and Eastern United States by seismic surface wave imaging. *Geophysical*
1527 *Research Letters*, 43(1), 118-126. <https://doi.org/10.1002/2015GL066637>.

1528 Pommier A., Kohlstedt, D. L., Hansen, L. N., Mackwell, S., Tasaka, M., Heidelbach, F., &
1529 Leinenweber, K. (2018). Transport properties of olivine grain boundaries from electrical
1530 conductivity experiments. *Contributions to Mineralogy and Petrology*, 173, 41.
1531 <https://doi.org/10.1007/s00410-018-1468-z>.

1532 Portenga, E. W., & Bierman, P. R. (2011). Understanding Earth’s eroding surface with 10Be. *GSA*
1533 *Today*, 21(8), 4-10. <https://doi.org/10.1130/G111.A1>.

1534 Portenga, E. W., Bierman, P. R., Trodick, C. D., Greene, S. E., DeJong, B. D., Rood, D. H., &
1535 Pavich, M. J. (2019). Erosion rates and sediment flux within the Potomac River basin
1536 quantified over millennial timescales using beryllium isotopes. *Geological Society of America*
1537 *Bulletin*, 131(7-8), 1295-1311. <https://doi.org/10.1130/B31840.1>.

1538 Porter, R., Liu, Y., & Holt, W.E., (2016). Lithospheric records of orogeny within the continental
1539 US. *Geophysical Research Letters*, 43, 144–153. <https://doi.org/10.1002/2015GL066950>

1540 Pozgay, S. H., Wiens, D. A., Conder, J. A., Shiobara, H., & Sugioka, H. (2009). Seismic
1541 attenuation tomography of the Mariana subduction system: Implications for thermal structure,
1542 volatile distribution, and slow spreading dynamics. *Geochemistry, Geophysics, Geosystems*,
1543 10, Q04X05. <https://doi.org/10.1029/2008GC002313>.

1544 Pratt, T. L., Çoruh, C., Costain, J. K., & Glover III, L. (1988). A geophysical study of the Earth’s
1545 crust in central Virginia: Implications for Appalachian crustal structure. *Journal of*
1546 *Geophysical Research: Solid Earth*, 93, 6649-6667. <https://doi.org/10.1029/JB093iB06p06649>.

1548 Rowley, D. B., Forte, A. M., Moucha, R., Mitrovica, J. X., Simmons, N. A., & Grand, S. P. (2013).
1549 Dynamic topography change of the eastern United States since 3 million years ago. *Science*,
1550 340,1560–1563. <https://doi.org/10.1126/science.1229180>

1551 Sarafian, E., Gaetani, G. A., Hauri, E. H., & Sarafian, A. R. (2017). Experimental constraints on
1552 the damp peridotite solidus and oceanic mantle potential temperature. *Science*, 355, 942–945.
1553 <https://doi.org/10.1126/science.aaj2165>.

1554 Savage, B. (2021). Body wave speed structure of Eastern North America. *Geochemistry,*
1555 *Geophysics, Geosystems*, 22, e2020GC009002. <https://doi.org/10.1029/2020GC009002>.

1556 Savage, B., Covellone, B.M. & Shen, Y. (2017). Wave speed structure of the eastern North
1557 American margin. *Earth and Planetary Science Letters*, 459, 394-405.

1558 Schaeffer, A.J. and Lebedev, S., 2014. Imaging the North American continent using waveform
1559 inversion of global and USArray data. *Earth and Planetary Science Letters*, 402, pp.26-41.
1560 <https://doi.org/10.1016/j.epsl.2016.11.028>.

1561 Schmandt, B., Dueker, K., Humphreys, E., & Hansen, S. (2012). Hot mantle upwelling across the
1562 660 beneath Yellowstone. *Earth and Planetary Science Letters*, 331-332, 224-236.
1563 <https://doi.org/10.1016/j.epsl.2012.03.025>.

1564 Schmandt, B., & Lin, F.-C. (2014). P and S wave tomography of the mantle beneath the United
1565 States. *Geophysical Research Letters*, 41, 6342–6349. [https://doi.org/10.1002/](https://doi.org/10.1002/2014GL061231)
1566 [2014GL061231](https://doi.org/10.1002/2014GL061231).

1567 Schmandt, B., Lin, F.-C., & Karlstrom, K.E. (2015). Distinct crustal isostasy trends east and west
1568 of the Rocky Mountain Front. *Geophysical Research Letters*, 42(23), 10,290-10,298.
1569 <https://doi.org/10.1002/2015GL066593>.

1570 Shen, W. & Ritzwoller, M.H. (2016). Crustal and uppermost mantle structure beneath the United
1571 States. *Journal of Geophysical Research: Solid Earth*, 121(6), 4306-4342.
1572 <https://doi.org/10.1002/2016JB012887>.

1573 Shorten, C. M., & Fitzgerald, P. G. (2021). Episodic exhumation of the Appalachian orogen in the
1574 Catskill Mountains (New York State, USA). *Geology*, 49(5), 571-575.
1575 <https://doi.org/10.1130/G48011.1>.

1576 Sifré, D., Gardés, E., Massuyeua, M., Hashim, L., Hier-Majumder, S., & Gaillard, F. (2014). The
1577 electrical conductivity during incipient melting in the oceanic low velocity zone. *Nature*, 509,
1578 81-85. <https://doi.org/10.1038/nature13245>.

1579 Smyth, J. R., & Frost, D. J. (2002). The effect of water on the 410-km discontinuity: An experimental
1580 study. *Geophysical Research Letters*, 29, 1485. <https://doi.org/10.1029/2001GL014418>.

1581 Soles, B., Brennan, G., Johnson, E., Mazza, S., & Gazel, E. (2014). Variable water concentrations
1582 in the asthenospheric and lithospheric mantle underneath the Eastern United States. AGU Fall
1583 Meeting, San Francisco, CA, abstract ED31F-3491.

1584 Southworth, C. S., Gray, K. J., & Sutter, J.S. (1993). Middle Eocene intrusive igneous rocks of the
1585 central Appalachian Valley and Ridge Province — Setting, chemistry, and implications for
1586 crustal structure. *U.S. Geological Survey Bulletin*, Report B1839-I, J1–J24.

1587 Spasojevic, S., Liu, L., Gurnis, M., & Müller, R. D. (2008). The case for dynamic subsidence of
1588 the U.S. east coast since the Eocene. *Geophysical Research Letters*, 35, L08305.
1589 <https://doi.org/10.1029/2008GL033511>.

1590 Spotila, J. A., Bank, G. C., Reiners, P. W., Naeser, C. W., Naeser, N. D., & Henika, B. S. (2004).
1591 Origin of the Blue Ridge escarpment along the passive margin of Eastern North America. *Basin*
1592 *Research*, 16, 41-63. <https://doi.org/10.1111/j.1365-2117.2003.00219.x>.

1593 Stein, C. A., Stein, S., Merino, M., Keller, G. R., Flesch, L. M., & Jurdy, D. M. (2014). Was the
1594 Midcontinent Rift part of a successful seafloor-spreading episode? *Geophysical Research*
1595 *Letters*, 41, 1465-1470. <https://doi.org/10.1002/2013GL059176>.

1596 Takei, Y., (2017). Effects of partial melting on seismic velocity and attenuation: A new insight
1597 from experiments. *Annual Review of Earth and Planetary Sciences*, 45, 447–470.
1598 <https://doi.org/10.1146/annurev-earth-063016-015820>.

1599 Thomas, W. A., & Powell, C. A. (2017). Necessary conditions for intraplate seismic zones in North
1600 America. *Tectonics*, 36, 2903-2917. <https://doi.org/10.1002/2017TC004502>.

1601 Till, C. B., Elkins-Tanton, L. T., & Fischer, K. M. (2010). A mechanism for low-extent melts at
1602 the lithosphere-asthenosphere boundary. *Geochemistry, Geophysics, Geosystems*, 11, Q10015.
1603 <https://doi.org/10.1029/2010GC003234>.

1604 Tso, J.L., & Surber, J.D. (2006). Eocene igneous rocks near Monterey, Virginia; A field study.
1605 *Virginia Minerals*, 48, 25–40.

1606 Turcotte, D. L., & Schubert, G. (2002). *Geodynamics*. Cambridge, UK: Cambridge University
1607 Press.

1608 van der Lee, S., & A. Frederiksen (2005), Surface wave tomography applied to the North America
1609 upper mantle, in *Seismic Earth: Array Analysis of Broadband Seismograms*, edited by G. Nolet
1610 and A. Levander, pp.67-80, American Geophysical Union, Washington, DC.

1611 Van der Lee, S., Regenauer-Lieb, K., & Yuen, D. (2008). The role of water in connecting past and
1612 future episodes of subduction. *Earth and Planetary Science Letters*, 273, 15-27,
1613 <https://doi.org/10.1016/j.epsl.2008.04.041>.

1614 Van Wijk, J., Baldrige, S., van Hunen, J., Goes, S., Aster, R., Coblenz, D., Grand, S., & Ni, J.
1615 (2010). Small-scale convection at the edge of the Colorado Plateau: Implications for
1616 topography, magmatism, and evolution of Proterozoic lithosphere. *Geology*, 38, 611-614.
1617 <https://doi.org/10.1130/G31031.1>.

1618 Wagner, L. S., Stewart, K., & Metcalf, K. (2012). Crustal-scale shortening structures beneath the
1619 Blue Ridge Mountains, North Carolina, USA. *Lithosphere*, 4, 242-256.
1620 <https://doi.org/10.1130/L184.1>.

1621 Wagner, L. S., Fischer, K. M., Hawman, R., Hopper, E., & Howell, D. (2018). The relative roles
1622 of inheritance and long-term passive margin lithospheric evolution on the modern structure
1623 and tectonic activity in the southeastern United States. *Geosphere*, 14, 1385-1410.
1624 <https://doi.org/10.1130/GES01593.1>.

1625 Wang, H., Zhao, D., Huang, Z. & Wang, L. (2019). Tomography, seismotectonics, and mantle
1626 dynamics of central and eastern United States. *Journal of Geophysical Research: Solid Earth*,
1627 124(8), 8890-8907. <https://doi.org/10.1029/2019JB017478>.

1628 Wang, Y., & Pavlis, G. L. (2016). Roughness of the mantle transition zone discontinuities revealed
1629 by high-resolution wavefield imaging. *Journal of Geophysical Research: Solid Earth*, 121(9),
1630 6757-6778. <https://doi.org/10.1002/2016JB013205>.

1631 Waring, G. A. (1965). Thermal springs of the United States and other countries of the world: A
1632 summary. *U. S. Geological Survey Professional Paper*, 492.

1633 Wei, S., & Wiens, D. A. (2018). P-wave attenuation structure of the Lau back-arc basin and
1634 implications for mantle wedge processes. *Earth and Planetary Science Letters*, 502, 187-199.
1635 <https://doi.org/10.1016/j.epsl.2018.09.005>.

1636 Wei, W., & Wiens, D. A. (2020). High bulk and shear attenuation due to partial melt in the Tonga-
1637 Lau back-arc mantle. *Journal of Geophysical Research: Solid Earth*, 125, e2019JB017527.
1638 <https://doi.org/10.1029/2019JB017527>.

1639 Whalen, L., Gazel, E., Vidito, C., Puffer, J., Bizimis, M., Henika, W., & Caddick, M.J. (2015).
1640 Supercontinental inheritance and its influence on supercontinental breakup: The Central
1641 Atlantic Magmatic Province and the breakup of Pangea. *Geochemistry, Geophysics,*
1642 *Geosystems*, 16, 3532–3554. <https://doi.org/10.1002/2015GC005885>.

1643 Whipple, K.X., & Tucker, G.E. (1999). Dynamics of the stream-power river incision model:
1644 implications for height limits of mountain ranges, landscape response timescales, and research
1645 needs. *Journal of Geophysical Research: Solid Earth*, 104, 17661-17674.
1646 <https://doi.org/10.1029/1999JB00120>.

1647 Whitmeyer, S., & Karlstrom, K. (2007). Tectonic model for the Proterozoic growth of North
1648 America. *Geosphere*, 3, 220-259. <https://doi.org/10.1130/GES00055.1>.

- 1649 Wobus, C., Whipple, K. X., Kirby, E., Snyder, N., Johnson, J., Spyropolou, K., Crosby, B., &
1650 Sheehan, D. (2006). Tectonics from topography: Procedures, promise, and pitfalls, in: Willett,
1651 S. D., Hovius, N., Brandon, M. T., & Fisher, D. (Eds.), *Tectonics, Climate, and Landscape*
1652 *Evolution*. Geological Society of America, Boulder, Colorado, pp. 55-74.
- 1653 Williams, M. L., Dumond, G., Mahan, K., Regan, S., & Holland, M. (2014). Garnet-forming
1654 reactions in felsic orthogneiss: Implications for densification and strengthening of the lower
1655 continental crust. *Earth and Planetary Science Letters*, 405, 207-219. [https://doi.org/](https://doi.org/10.1016/j.epsl.2014.08.030)
1656 [10.1016/j.epsl.2014.08.030](https://doi.org/10.1016/j.epsl.2014.08.030).
- 1657 Withjack, M. O., Schlische, R. W., & Olsen, P. E. (1998). Diachronous rifting, drifting, and
1658 inversion on the passive margin of Central Eastern North America: An analog for other passive
1659 margins. *AAPG Bulletin*, 82, 817-835.
- 1660 Withjack, M. O., Schlische, R. W., & Olsen, P. E. (2012). Development of the passive margin of
1661 Eastern North America: Mesozoic rifting, igneous activity, and breakup. *Regional Geology*
1662 *and Tectonics: Phanerozoic Rift Systems and Sedimentary Basins*, 1b, 301-335.
- 1663 Wolin, E., Stein, S., Pazzaglia, F., Meltzer, A., Kafka, A., & Berti, C. (2012). Mineral, Virginia
1664 earthquake illustrates seismicity of a passive-aggressive margin. *Geophysical Research*
1665 *Letters*, 39, L02305. <https://doi.org/10.10129/2011GL050310>.
- 1666 Wright, N. M., Müller, R. D., Seton, M., & Williams, S. E. (2015). Revision of Paleogene plate
1667 motions in the Pacific and implications for the Hawaiian-Emperor bend. *Geology*, 43, 455-
1668 458. <http://doi.org/10.1130/G36303.1>.
- 1669 Xie, J., Chu, R., & Yang, Y. (2018). 3-D upper-mantle shear velocity model beneath the contiguous
1670 United States based on broadband surface wave from ambient seismic noise. *Pure and Applied*
1671 *Geophysics*, 175(10), 3403-3418. <https://doi.org/10.1007/s00024-018-1881-2>.
- 1672 Yamauchi, H., & Takei, Y. (2016). Polycrystal anelasticity at near-solidus temperatures. *Journal*
1673 *of Geophysical Research: Solid Earth*, 121, 2016JB013316. [https://doi.org/10.1002/](https://doi.org/10.1002/1202016JB013316)
1674 [1202016JB013316](https://doi.org/10.1002/1202016JB013316).
- 1675 Yang, Y., & Forsyth, D. W. (2006). Regional tomographic inversion of the amplitude and phase
1676 of Rayleigh waves with 2-D sensitivity kernels. *Geophysical Journal International*, 166, 1148-
1677 1160. <https://doi.org/10.1111/j.1365-246X.2006.02972.x>.
- 1678 Yang, B. B., Liu, Y., Dahm, H., Liu, K. H., & Gao, S. S. (2017). Seismic azimuthal anisotropy
1679 beneath the eastern United States and its geodynamic implications. *Geophysical Research*
1680 *Letters*, 44, 2670–2678. <https://doi.org/10.1002/2016GL071227>.
- 1681 Yoshino, T., Laumonier, M., McIsaac, E., & Katsura, T. (2010). Electrical conductivity of basaltic
1682 and carbonatite melt-bearing peridotites at high pressures: Implications for melt distribution
1683 and melt fraction in the upper mantle. *Earth and Planetary Science Letters*, 295, 593-602.
1684 <https://doi.org/10.1016/j.epsl.2010.04.050>.
- 1685 Yuan, H., French, S., Cupillard, P., & Romanowicz, B. (2014). Lithospheric expression of
1686 geological units in central and eastern North America from full waveform tomography. *Earth*
1687 *and Planetary Science Letters*, 402, 176-186. <https://doi.org/10.1016/j.epsl.2013.11.057>.

1688 1689 1690 **Supporting Information References**

- 1691
1692 Bierman, P., & Steig, E.J. (1996). Estimating rates of denudation using cosmogenic isotope
1693 abundances in sediment. *Earth Surface Processes and Landforms*, 21, 125-139.
1694 [https://doi.org/10.1002/SICI/1096-9837\(199602\)21:2<125::AID-ESP511>3.0.CO;2-8](https://doi.org/10.1002/SICI/1096-9837(199602)21:2<125::AID-ESP511>3.0.CO;2-8).

1695 Granger, D.E., Kirchner, J.W., & Finkel, R. (1996). Spatially averaged long-term erosion rates
1696 measured from in situ-produced cosmogenic nuclides in alluvial sediment. *Journal of Geology*,
1697 *104*, 249-257. <https://doi.org/10.1086/629823>.

1698 Greene, C. A., Thirumalai, K., Kearney, K. A., Delgado, J. M., Schwanghart, W., Wolfenbarger,
1699 N. S., & Blankenship, D. D. (2019). The climate data toolbox for MATLAB. *Geochemistry*,
1700 *Geophysics, Geosystems*, *20*(7), 3774-3781. <https://doi.org/10.1029/2019GC008392>.

1701 Schwanghart, W., & Scherler, D. (2014). TopoToolbox 2–MATLAB-based software for
1702 topographic analysis and modeling in Earth surface sciences. *Earth Surface Dynamics*, *2*(1),
1703 1-7. <https://doi.org/10.5194/esurf-2-1-2014>.

1704 Schwanghart, W., & Scherler, D. (2017). Bumps in river profiles: uncertainty assessment and
1705 smoothing using quantile regression techniques. *Earth Surface Dynamics*, *5*, 821-839.
1706 <https://doi.org/10.5194/esurf-5-821-2017>.

1707 Thirumalai, K., Singh, A., & Ramesh, R. (2011). A MATLAB code to perform weighted linear
1708 regression with (correlated or uncorrelated) errors in bivariate data. *Journal of the Geological*
1709 *Society of India*, *77*(4), 377-380. <https://doi.org/10.1007/s12594-011-0044-1>.

1710 Trappitsch, R., Boehnke, P., Stephan, T., Telus, M., Savina, M. R., Pardo, O., et al., (2018). New
1711 constraints on the abundance of ⁶⁰Fe in the early solar system. *The Astrophysical Journal*
1712 *Letters*, *857*(2), L15. <https://doi.org/10.3847/2041-8213/aabba9>.

1713 York, D., Evensen, N. M., Martinez, M. L., & De Basabe Delgado, J. (2004). Unified equations
1714 for the slope, intercept, and standard errors of the best straight line. *American Journal of*
1715 *Physics*, *72*(3), 367-375. <https://doi.org/10.1119/1.1632486>
1716
1717

1718

1719

1720

1721

1722

1723

1724

1725

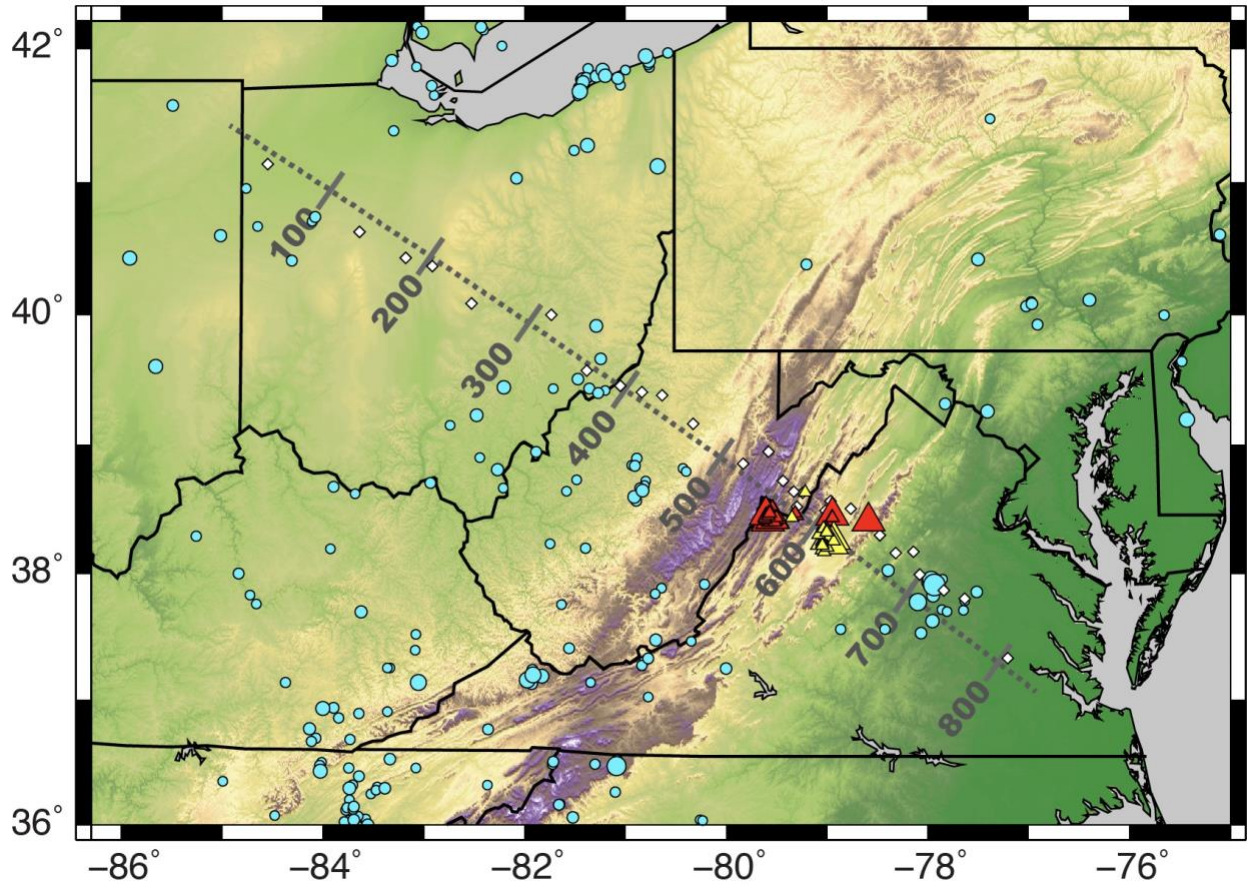
1726

1727

1728

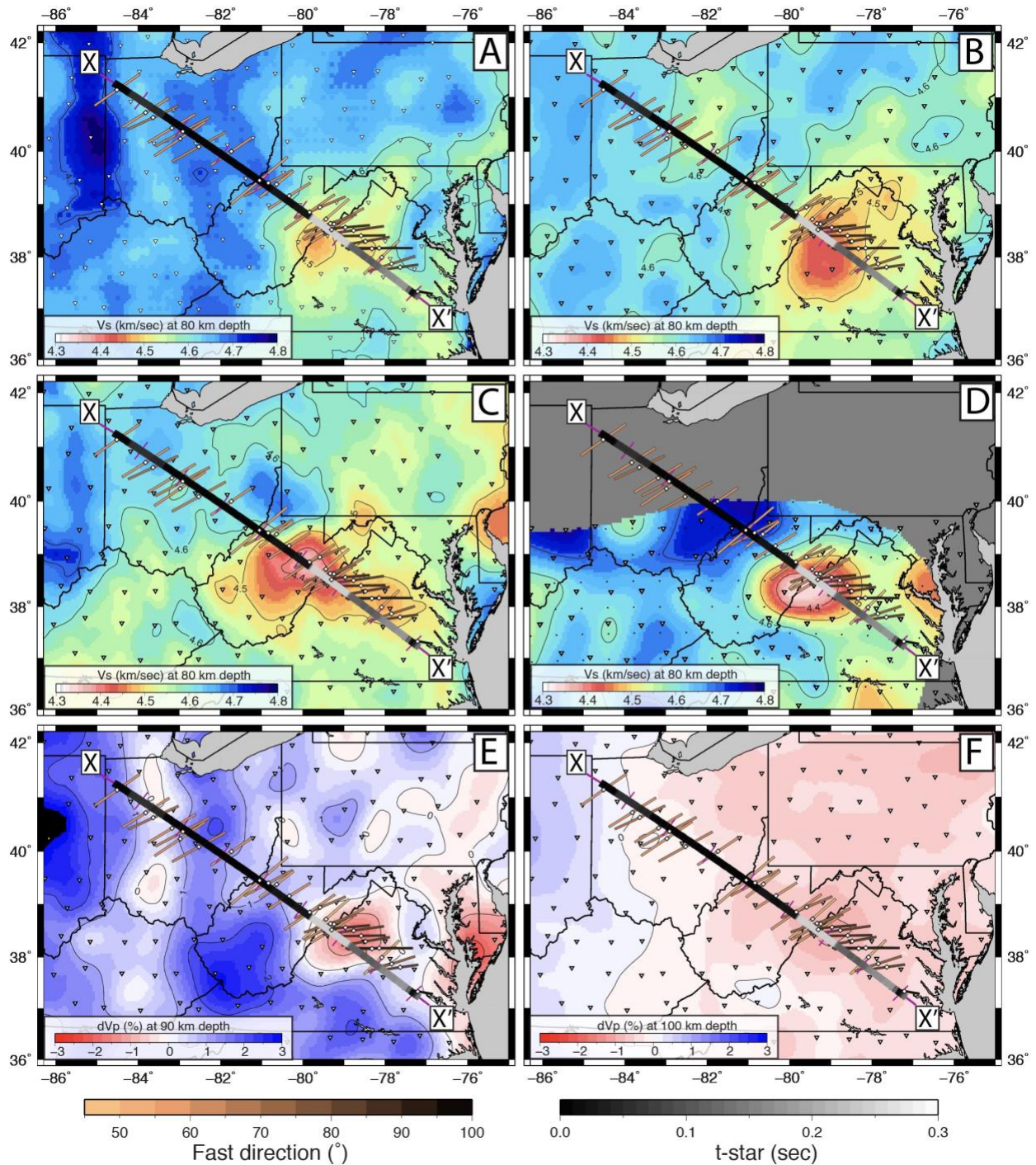
1729 **Figures and Captions**

1730



1731

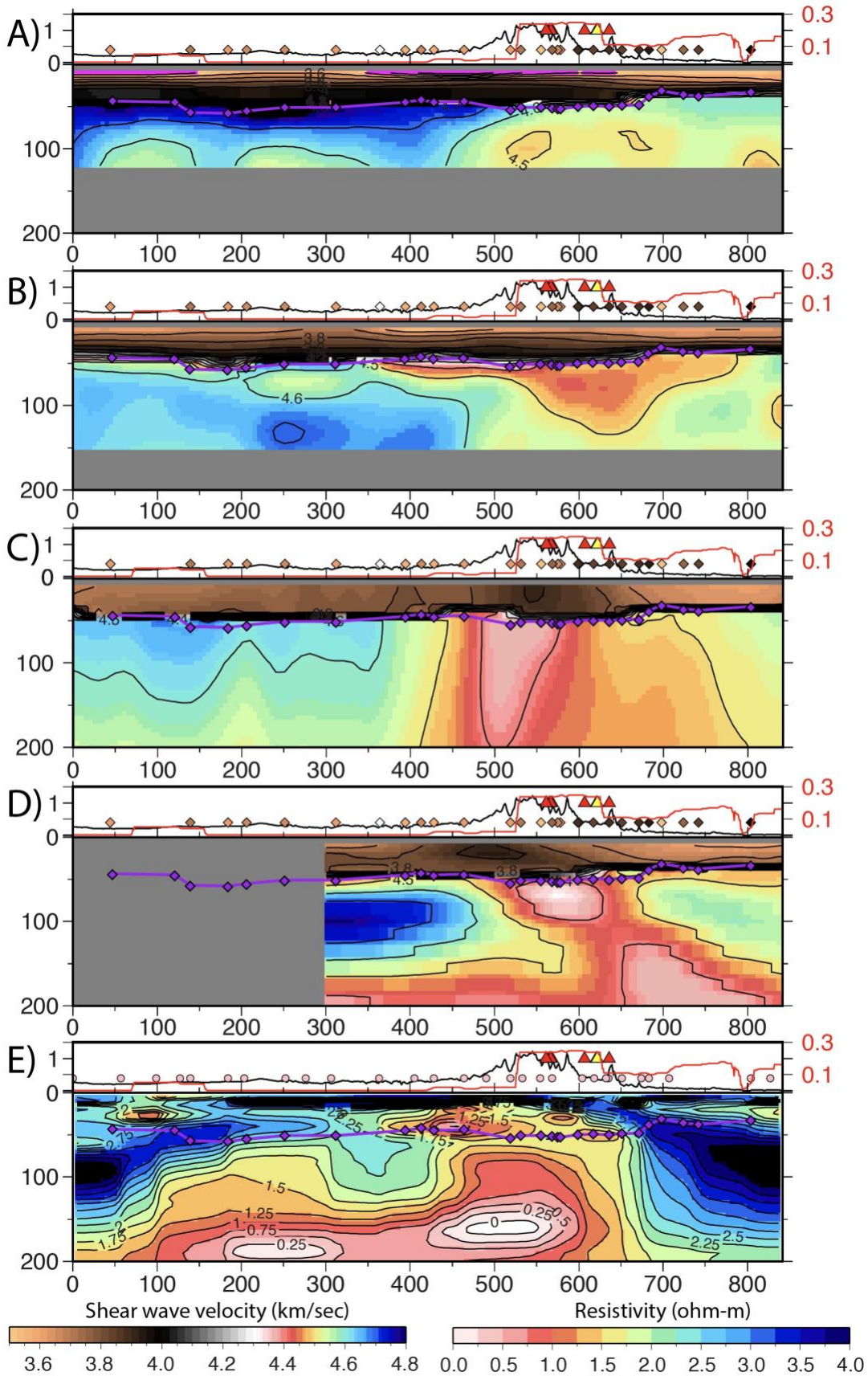
1732 Figure 1. Map of study area. Background color shows topography. Triangle show locations of
1733 post-CAMP volcanism (Mazza et al., 2017). Larger triangles are samples with age constraints. Red
1734 triangles are Eocene, yellow triangles are Jurassic. Blue circles indicate seismicity from the NEIC
1735 catalog, 2001-2021 with $M > 2.5$. Grey dotted line indicates location of cross-section shown in
1736 Figures 2 and 3. Tick marks show 100 km increments along that profile from NW to SE. White
1737 diamonds show locations of MAGIC stations.



1738

1739 **Figure 2:** Seismic constraints on upper mantle structure in map view. Background colors show
 1740 different tomographic models. A-D show absolute shear wave velocities from surface wave studies
 1741 at 80 km depth, contoured at 0.1 km/sec: A) Schmandt et al. (2015); B) Shen & Ritzwoller, (2016);
 1742 C) Porter et al. (2016); D) Wagner et al. (2018). Panels E & F show P-wave velocity deviations

1743 determined from teleseismic travel time residuals contoured every 1% increment: E) at 90 km
1744 depth by Schmandt & Lin (2014); F) at 100 km depth by Boyce et al. (2019). Triangles show
1745 locations of EarthScope Transportable Array stations. For D) only stations used in the inversion
1746 are shown. Small black dots in D) show inversion grid node locations. Transect X-X' shown in
1747 purple with purple tick marks every 100 km from N-S shows location of the cross section in Figure
1748 3. Superimposed on the transect is the projection of t^* measurements from Byrnes et al. (2019).
1749 SKS splitting measurements from Aragon et al. (2017) at MAGIC stations (diamonds) are shown
1750 as bars color coded by fast direction in degrees clockwise from north.



1752 **Figure 3:** Cross-sections along X-X' as shown in Figure 2. At the top of each panel, black line
1753 shows topography, red line shows t^* measurements of Byrnes et al. (2019), red triangles show the
1754 locations of Eocene volcanism, and yellow triangle shows Jurassic volcanism (Mazza et al., 2017).
1755 In Panels A-D, diamonds show projected locations of MAGIC stations color coded by fast splitting
1756 directions using the same color scale used in Figure 2. Panel E shows the locations of MT stations
1757 used in Evans et al. (2019). Models A-D correspond to the same seismic velocity models in A-D
1758 in Figure 2: A) Schmandt et al. (2015); B) Shen & Ritzwoller (2016); C) Porter et al. (2016); D)
1759 Wagner et al. (2018). Colors show shear wave velocities in km/sec. Panel E shows the electrical
1760 resistivity model of Evans et al. (2019). In all panels, purple line and purple diamonds show
1761 estimates of Moho depths determined from Ps receiver function analysis from Long et al. (2019).

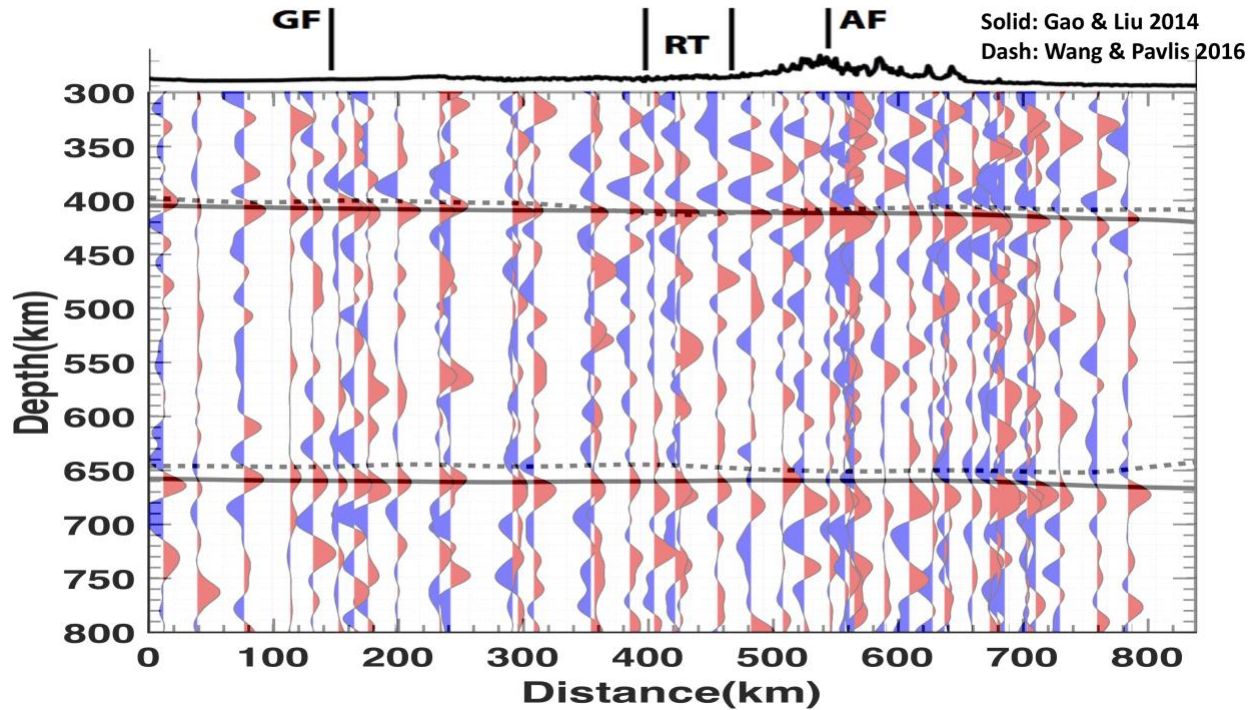
1762

1763

1764

1765

1766



1767

1768

1769

1770 Figure 4. Image of Ps conversions from transition zone discontinuities beneath the MAGIC line

1771 (Liu et al., 2018). Radial component Ps receiver function traces have been stacked at individual

1772 stations, migrated to depth using a standard Earth model (iasp91; Kennett & Engdahl, 1991), and

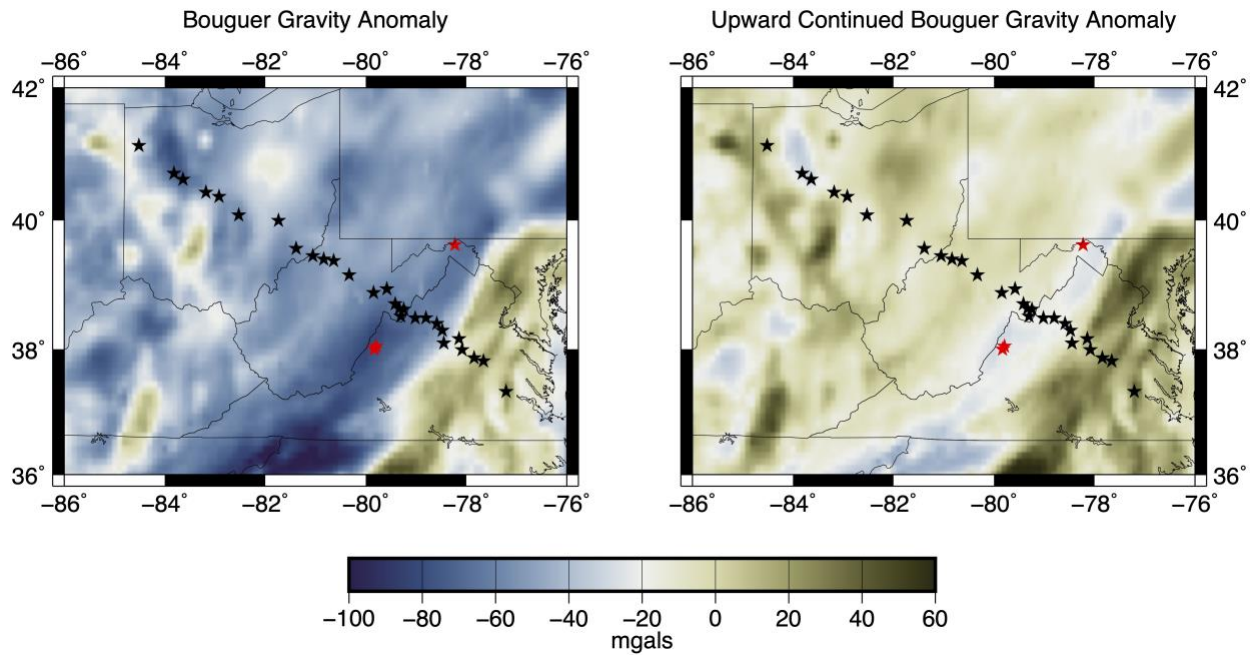
1773 plotted as a function of distance along the MAGIC profile (as shown in Figure 1). Red pulses

1774 indicate a conversion due to a discontinuity with a positive velocity gradient, as expected for the

1775 410 and 660 km discontinuities. Liu et al. (2018) observed a generally constant transition zone

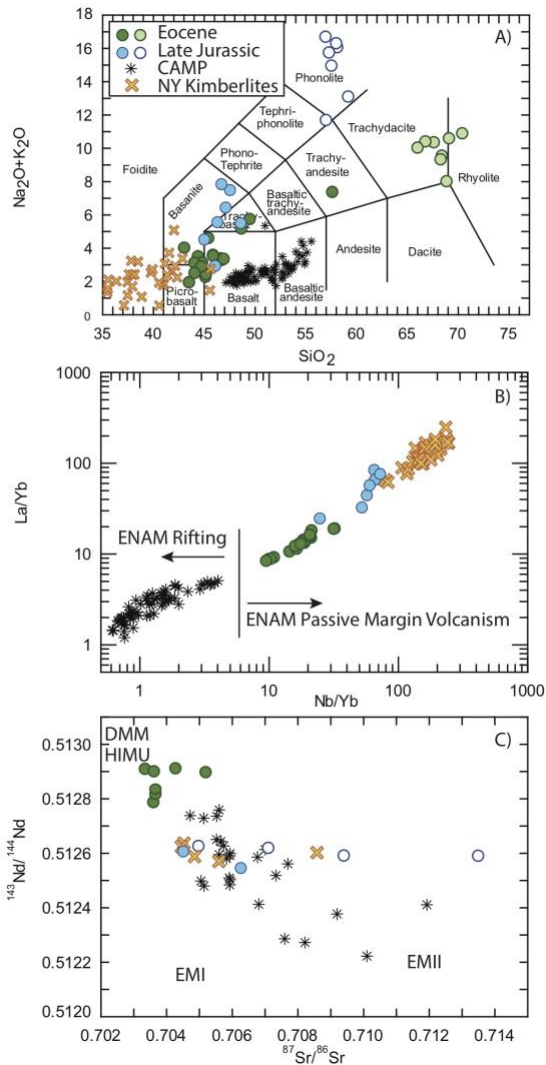
1776 thickness across the MAGIC line, consistent with imaging by Gao and Liu (2014; solid line) and

1777 Pavlis et al. (2016; dashed line) using data from TA stations.



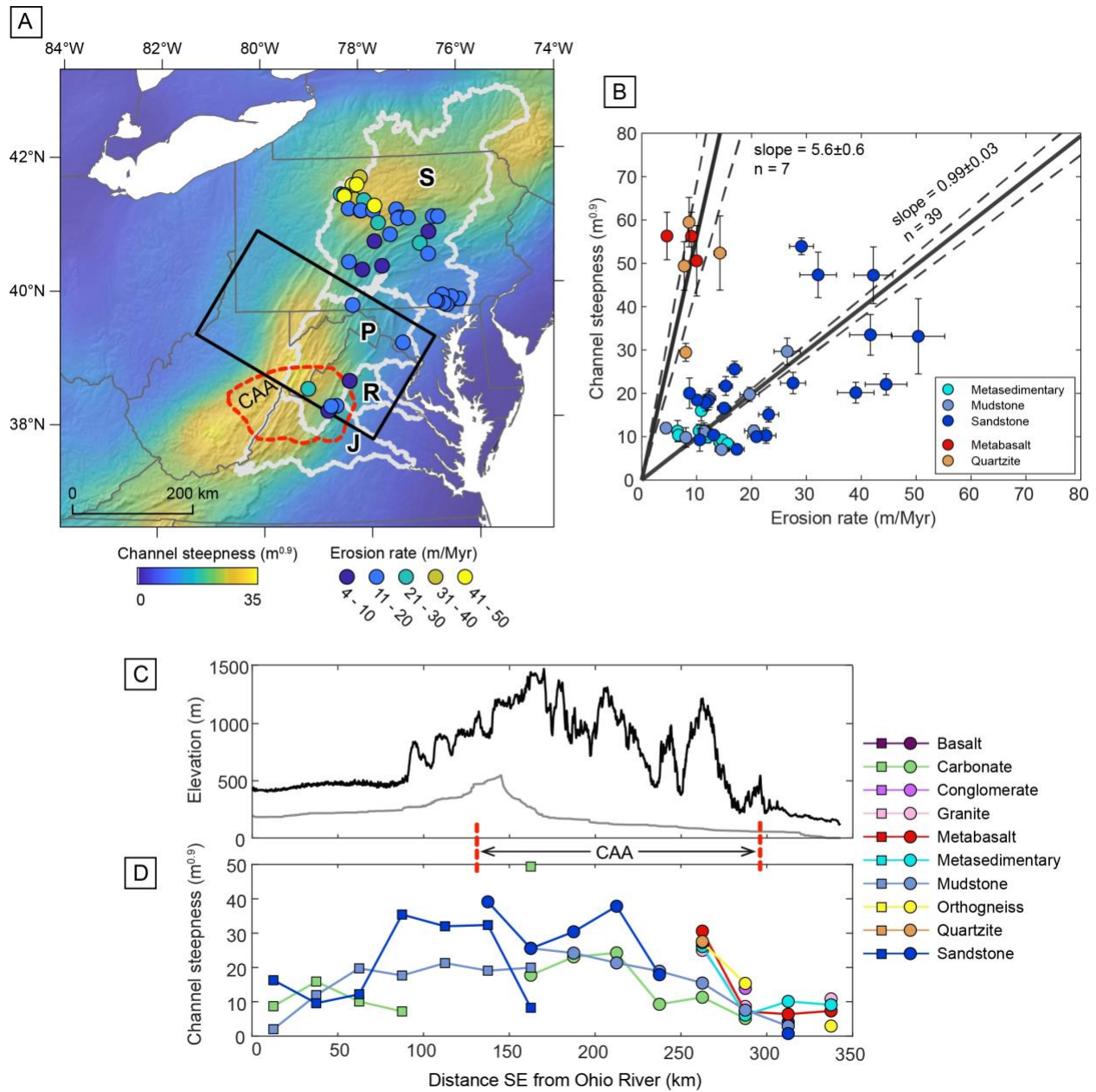
1778

1779 Figure 5. Gravity anomaly maps of the Central Appalachians. Left panel shows Bouguer gravity
 1780 anomaly from PACES, while right panel shows a reduced Bouguer gravity anomaly map obtained
 1781 following Stein et al. (2014). We upward continued the Bouguer anomaly data to 40 km and
 1782 subtracted the result from the original Bouguer anomaly data. Black stars show the locations of
 1783 MAGIC stations, while red stars show locations of prominent hot springs.



1784

1785 Figure 6. A) Total alkalis (Na₂O v+ K₂O) versus SiO₂ for the eastern North American Margin
 1786 (ENAM) volcanics including the Virginia-West Virginia Late Jurassic and Eocene volcanic pulses
 1787 showing bimodal populations (Mazza et al., 2014, 2017), the Central Atlantic Magmatic Province
 1788 (CAMP, Callegaro et al., 2013; Whalen et al., 2015), and the New York (NY) kimberlites (Bailey
 1789 & Lupulescu, 2015). B) La/Yb versus Nb/Yb showing differences in eastern North American
 1790 Margin (ENAM) rifting and passive margin volcanics. C) ¹⁴³Nd/¹⁴⁴Nd versus ⁸⁷Sr/⁸⁶Sr for ENAM
 1791 volcanics. DMM – depleted MORB mantle, EMI – enriched mantle I, EMII- enriched mantle II,
 1792 HIMU – high ²³⁸U/²⁰⁴Pb mantle.



1793

1794 Figure 7. Topography and erosion rates in the Central Appalachians. A.) Map of study area

1795 showing smoothed channel steepness indices throughout study area. Red dashed line shows the

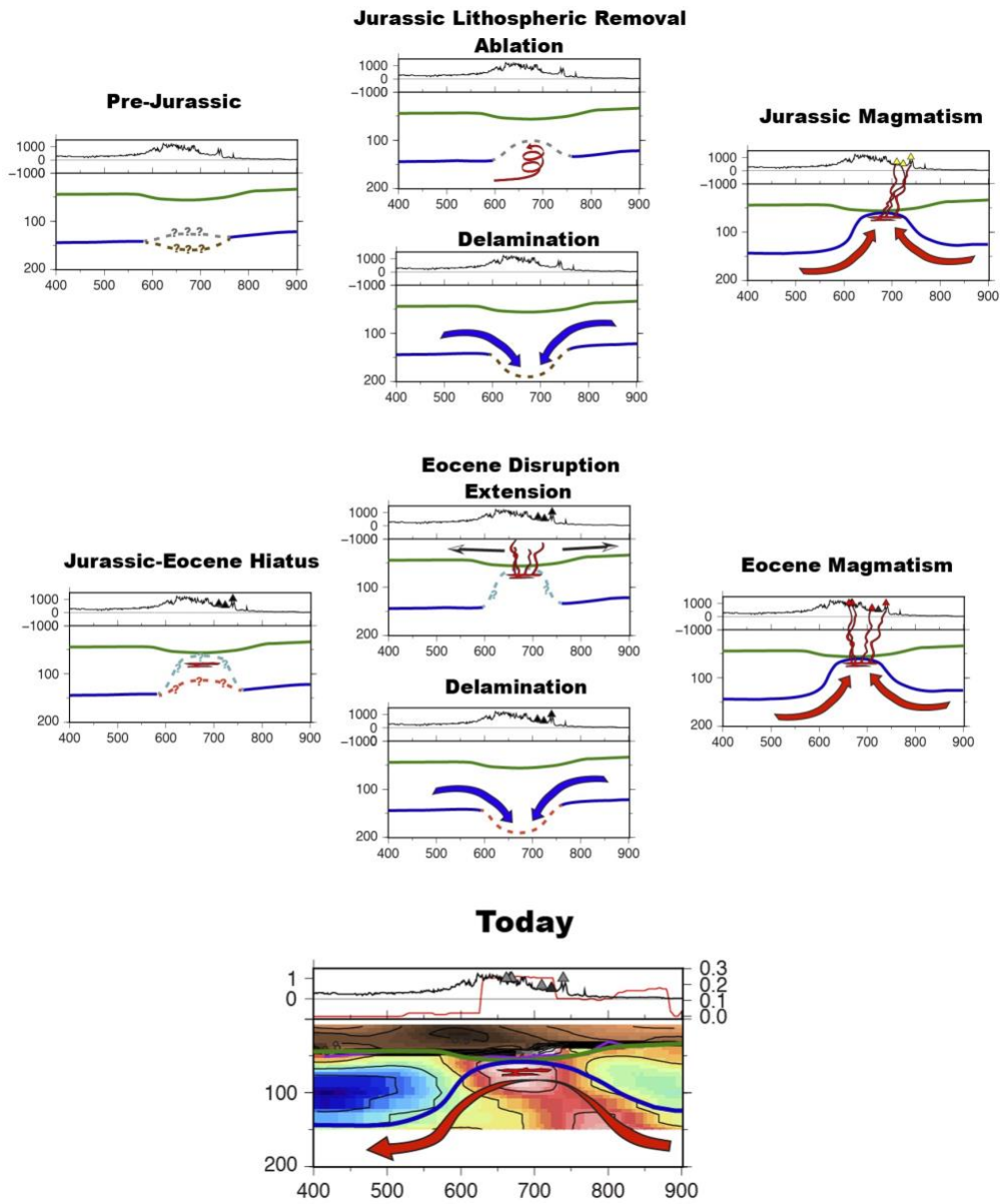
1796 approximate outline of the CAA based on the 4.5 km/s contour in Wagner et al., 2018 (see Figure

1797 2D), and black rectangle outlines the swath profiles shown in C and D. Colored circles represent

1798 locations of erosion rate samples used in the analysis (see text for details). Watershed boundaries

1799 of major rivers shown in white; J-James, R-Rappahannock, P-Potomac, S-Susquehanna. B.)

1800 Scaling relationships among channel steepness, erosion rate, and lithology for basins throughout
1801 the central Appalachian region. Results of York regressions forced through origin characterize
1802 two separate groups of rock type; 2σ bounds shown with dashed lines. C.) Maximum (black) and
1803 minimum (gray) elevations along the swath profile. D.) Mean values of channel steepness along
1804 the swath profile separated by rock type and drainage direction. Channels west of the drainage
1805 divide are shown with square symbols, and channels east of the divide are shown with circles.
1806



1807

1808 Figure 8. Schematic cartoon of possible scenarios for lithospheric removal and evolution from the
 1809 Jurassic to the present. Top set of panels shows possible configurations and processes during the
 1810 Jurassic (including pre-removal, during lithospheric removal, and during magmatism), middle set
 1811 of panels shows possible configurations and processes during the Eocene (including during the

1812 Jurassic-Eocene hiatus, during lithospheric removal, and during magmatism), and the bottom panel
1813 shows the present-day configuration. In all panels, the green line indicates the possible Moho
1814 architecture and the blue line indicates the possible LAB geometry; lines are dashed where
1815 uncertainty is particularly high. Red colors indicate the likely presence of melt, arrows indicate
1816 possible (highly schematic) flow scenarios, and triangles indicate magmatic products at surface.
1817 In the lower panel, plotting conventions and velocity models are as in Figure 3d. Present-day
1818 topography is shown at the top of all panels for reference.

1819

1820

1821

Supporting Information for**Evaluating models for lithospheric loss and intraplate volcanism beneath the Central Appalachian Mountains**

Maureen D. Long¹, Lara S. Wagner², Scott D. King³, Rob L. Evans⁴, Sarah E. Mazza⁵, Joseph S. Byrnes^{6,7}, Elizabeth A. Johnson⁸, Eric Kirby⁹, Maximiliano J. Bezada⁶, Esteban Gazel¹⁰, Scott R. Miller¹¹, John C. Aragon^{1,12}, Shangxin Liu³

¹Dept. Earth & Planetary Sciences, Yale University, New Haven, CT, USA

²Earth & Planets Laboratory, Carnegie Institution for Science, Washington, DC, USA

³Dept. Geosciences, Virginia Tech, Blacksburg, VA, USA

⁴Dept. Geology & Geophysics, WHOI, Woods Hole, MA, USA

⁵Dept. Geosciences, Smith College, Northampton, MA, USA

⁶Dept. Earth & Environmental Sciences, University of Minnesota, Minneapolis, MN, USA

⁷Dept. Geosciences, Northern Arizona University, Flagstaff, AZ, USA

⁸Dept. Geology & Environmental Science, James Madison University, Harrisonburg, VA, USA

⁹Dept. Geological Sciences, University of North Carolina at Chapel Hill, Chapel Hill, NC, USA

¹⁰Dept. Earth & Atmospheric Sciences, Cornell University, Ithaca, NY, USA

¹¹Dept. Geology & Geophysics, University of Utah, Salt Lake City, UT, USA

¹²Now at: Earthquake Science Center, U.S. Geological Survey, Menlo Park, CA, USA

Contents of this file

Text S1

Figure S1

Table S1

Introduction

The supporting information contains supplemental data and methodology related to the analysis of topography and erosion rates above the Central Appalachian Anomaly.

Text S1*Analysis of topography and erosion rates above the Central Appalachian Anomaly*

To evaluate the relationships among topography, erosion rate, and substrate lithology in the central Appalachians, we compiled previously published erosion rates from ¹⁰Be in modern sediment along tributaries in the three primary watersheds that drain the study area (Portenga & Bierman, 2011; Duxbury et al., 2015; Portenga et al., 2019). These data are considered to

represent basin-wide average erosion rates for the regions upstream of the sample (e.g., Granger et al., 1996; Bierman & Steig, 1996). We resampled 1-arc-second digital topographic data from the National Elevation Dataset to 3-arc-seconds for a nominal resolution of the final gridded topography of ~90m. These data were hydrologically conditioned and watersheds extracted in TopoToolbox, a suite of Matlab functions developed for geomorphic analyses (Schwanghart & Scherler, 2014). Channel longitudinal profiles were smoothed using quantile regression and the CRS algorithm of Schwanghart and Scherler (2017), using a smoothing parameter, K , of 10 and quantile, τ , of 0.5. Longitudinal profile smoothing was not extended across lithologic contacts or edges of features such as reservoirs, lakes, or dams in the medium-resolution National Hydrographic Dataset Plus version 2 (NHDPlus V2) data (<https://www.epa.gov/waterdata/get-nhdplus-national-hydrography-dataset-plus-data>).

To generate regional maps of channel steepness (Figure 7), the parameter k_{sn} was calculated on a pixel-by-pixel basis for all cells in the DEM with drainage areas greater than 1 km², using the equation

$$k_{sn} = S / A^{-\theta_{ref}} \quad (S1)$$

where S is slope, A is drainage area, and θ_{ref} is a reference concavity. For this analysis, we used a $\theta_{ref} = 0.45$, following observations that this is a representative concavity for channels in the study area (Miller et al. 2013). Areas identified as lakes, reservoirs, and dams in the medium-resolution NHD, as well as a 0.5 km buffer around each, were removed from the grid of channel steepness. The channel steepness grid was smoothed with a Gaussian low-pass filter with a cutoff wavelength of 200 km (Greene et al., 2019). This smoothing length-scale was chosen as to fall within the range of preferred flexural wavelengths (170-280 km) associated with Plio-Pleistocene warping of the Orangeburg Escarpment (Moucha & Reutenik, 2017).

Within the 63 individual basins where erosion rates have been measured (Table S1), channel steepness values were calculated using the integral, or χ , method (Harkins et al. 2007; Perron and Royden, 2013) on unsmoothed channel profiles. Channel steepness was measured for the trunk stream and each tributary with a drainage area larger than 0.1 km², with the final value being the weighted average, where weighting is assigned by square of the channel length in χ coordinate. Channel profiles were visually inspected to evaluate the presence of slope-break knickpoints that might represent transient or non-equilibrium conditions (e.g., Kirby and Whipple, 2012). These were excluded (Table S1) from the final regression analysis of channel steepness and erosion rate (Figure 7).

To characterize lithologic substrate within these basins, geologic unit descriptions and contact locations were taken from Dicken et al. (2005) and Nicholson et al. (2005). The major lithology within each unit (GIS field "LITH1") was assigned to make a more generic rock classification that we utilize to classify points in Figures S1 and 7.

Linear regression of channel steepness and erosion rate was performed on both the complete (Figure S1) and the reduced data set (Figure 7) using a weighted bivariate regression that accounts for uncertainties in both variables (York et al., 2004). This regression adopts the methods of Thirumalai et al. (2011) and Trappitsch et al. (2018) for forcing the solution through the origin. The regression code and associated documentation are available on GitHub (https://github.com/scottrmiller/yorkregress_forced).

Figure S1

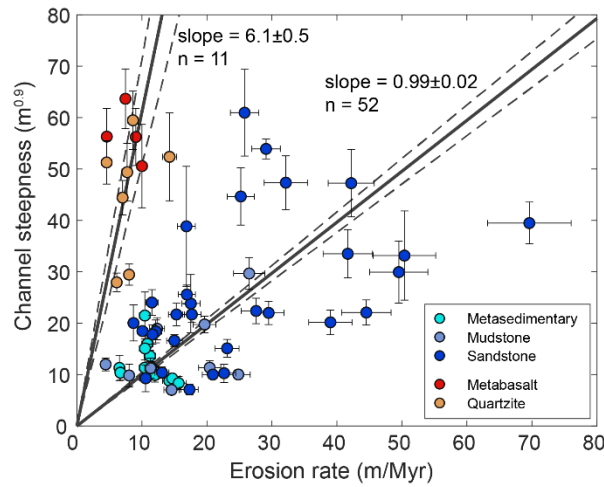


Figure S1. Channel steepness (k_{sn}) and erosion rate relationships for all basins in the study area.

Table S1

Table S1. Erosion rate sample locations and watershed metrics from upstream basins.

Basin ID ^A	Drainage basin ^B	Easting (m) ^C	Northing (m)	Elevation (m)	Dominant rock	Erosion rate (m/Myr)	k_{sn} ($m^{0.9}$)	Area (km)	Equilibrium flag ^D
JSQ100	Susq.	738047	4584417	296	Sandstone	32.14 ± 3.34	47.3 ± 5.2	3.0	1
JSQ102	Susq.	737789	4593594	346	Sandstone	69.6 ± 6.43	39.5 ± 4.1	3.3	0
JSQ103	Susq.	734633	4608264	386	Sandstone	41.67 ± 3.81	33.5 ± 4.7	5.7	1
JSQ104	Susq.	746512	4621169	544	Sandstone	39 ± 3.33	20.2 ± 2.4	3.6	1
JSQ105	Susq.	714656	4592882	549	Sandstone	22.65 ± 1.78	10.3 ± 1.8	3.1	1
JSQ106	Susq.	720585	4591886	492	Sandstone	27.57 ± 2.3	22.4 ± 2.5	3.2	1
JSQ107	Susq.	720688	4589638	437	Sandstone	44.52 ± 3.81	22.1 ± 2.4	3.3	1
JSQ108	Susq.	720962	4586067	499	Sandstone	17.68 ± 1.42	21.7 ± 1.6	5.2	0
JSQ109	Susq.	741377	4609163	474	Sandstone	50.39 ± 4.8	33.2 ± 8.7	3.3	1
JSQ111	Susq.	754584	4593323	372	Sandstone	16.85 ± 1.37	38.8 ± 11.7	5.6	0
JSQ112	Susq.	754952	4586030	342	Sandstone	49.52 ± 4.48	29.9 ± 6	3.4	0
JSQ113	Susq.	753434	4582971	445	Sandstone	23.11 ± 1.83	15.1 ± 1.7	3.8	1
JSQ114	Susq.	728079	4569483	574	Sandstone	13.09 ± 1.08	10.4 ± 1.1	6.4	1
JSQ115	Susq.	731860	4573171	481	Sandstone	17.53 ± 1.42	23.8 ± 5.7	4.7	0
JSQ116	Susq.	748293	4565600	415	Sandstone	15.3 ± 1.22	21.7 ± 2.2	6.5	1
JSQ117	Susq.	748673	4565921	420	Sandstone	15 ± 1.21	16.6 ± 1.2	3.3	1
JSQ118	Susq.	768837	4575357	328	Sandstone	25.8 ± 2.19	61 ± 8.4	4.0	0

JSQ119	Susq.	770757	4574247	368	Sandstone	42.2 ± 3.54	47.2 ± 6.5	5.6	1
JSQ120	Susq.	758110	4566515	287	Sandstone	25.21 ± 2.1	44.7 ± 5.6	15.5	0
JSQ123	Susq.	768474	4566321	580	Sandstone	11.62 ± 0.94	17.8 ± 1.9	2.6	1
JSQ124	Susq.	806851	4568033	211	Mudstone	12.33 ± 1.15	18.9 ± 2.2	2.6	1
JSQ125	Susq.	815274	4556335	377	Sandstone	29.5 ± 2.35	22 ± 2.3	9.8	0
JSQ126	Susq.	812940	4554905	507	Sandstone	20.91 ± 1.61	10 ± 0.5	2.2	1
JSQ127	Susq.	810155	4553009	511	Sandstone	10.57 ± 0.85	9.3 ± 2.6	5.5	1
JSQ128	Susq.	826250	4554266	433	Sandstone	16.91 ± 1.33	25.6 ± 1.8	3.2	1
JSQ130	Susq.	868285	4556417	165	Mudstone	14.56 ± 1.18	7 ± 0.6	6.1	1
JSQ131	Susq.	876224	4556798	193	Mudstone	19.64 ± 1.76	19.7 ± 1.6	5.2	1
JSQ132	Susq.	861111	4531129	167	Mudstone	8.03 ± 0.68	9.8 ± 2.2	4.0	1
JSQ133	Susq.	860361	4494424	407	Sandstone	10.08 ± 0.81	18.5 ± 0.8	3.0	1
JSQ134	Susq.	846587	4512145	137	Mudstone	20.43 ± 1.71	11.3 ± 1.3	5.5	1
JSQ135	Susq.	842081	4504952	128	Mudstone	24.83 ± 1.84	10 ± 0.9	4.2	0
JSQ136	Susq.	783865	4474081	265	Mudstone	4.42 ± 0.39	12 ± 1.2	3.0	1
JSQ140	Susq.	750828	4468137	371	Sandstone	8.7 ± 0.74	20 ± 3.5	3.3	1
JSQ141	Susq.	745434	4468675	393	Sandstone	11.54 ± 0.95	24 ± 2.5	4.6	0
JSQ142	Susq.	728770	4480379	284	Mudstone	11.34 ± 0.91	11.2 ± 2	2.7	1
JSQ143	Susq.	770107	4509898	397	Quartzite	6.12 ± 0.52	27.9 ± 1.8	3.6	0
JSQ144	Susq.	771083	4514664	503	Quartzite	8.02 ± 0.67	29.5 ± 2.1	3.1	1
JSQ146	Susq.	797099	4526095	517	Sandstone	17.32 ± 1.34	7.1 ± 1.1	3.1	1
JSQ149	Susq.	776948	4545630	250	Mudstone	26.5 ± 2.39	29.7 ± 3.1	3.0	1
JSQ150	Susq.	899798	4417344	67	Metasedimentary	11.25 ± 0.9	13.6 ± 1.1	4.0	0
JSQ151	Susq.	898866	4417918	112	Metasedimentary	6.54 ± 0.56	11.3 ± 2.5	3.4	1
JSQ152	Susq.	898393	4417641	133	Metasedimentary	6.69 ± 0.61	10.4 ± 1.5	3.1	1
JSQ153	Susq.	911843	4419808	131	Metasedimentary	14.67 ± 1.17	9.3 ± 0.5	25.5	1
JSQ154	Susq.	898883	4420059	67	Metasedimentary	10.45 ± 0.84	21.5 ± 4.6	5.3	0
JSQ155	Susq.	898616	4423299	113	Metasedimentary	10.85 ± 0.87	16 ± 2.3	4.0	1
JSQ156	Susq.	882950	4426180	188	Metasedimentary	12.14 ± 0.97	10.4 ± 1.2	4.3	1
JSQ157	Susq.	891136	4409935	149	Metasedimentary	15.65 ± 1.18	8.3 ± 1.3	4.0	1
JSQ158	Susq.	886018	4412505	149	Metasedimentary	11.44 ± 0.9	11.4 ± 1.1	6.9	1
JSQ159	Susq.	875031	4415483	236	Metasedimentary	10.44 ± 0.85	11.3 ± 1.5	7.6	1
JSQ160	Susq.	872188	4416384	214	Metasedimentary	12.01 ± 0.96	9.9 ± 1.4	3.7	1
JSQ161	Susq.	886824	4430423	126	Metasedimentary	10.47 ± 0.86	15.1 ± 3	3.4	0
POT18	Pot.	818514	4346631	119	Metasedimentary	14.2 ± 1.06	8.8 ± 0.5	13.5	1
POT45	Pot.	661008	4269318	703	Sandstone	29.1 ± 2.2	53.9 ± 1.9	29.4	1
POT64	Pot.	734901	4408831	217	Sandstone	12.15 ± 0.93	18.4 ± 2.2	12.6	1
SH02	Pot.	730110	4282751	380	Metabasalt	9.06 ± 0.75	56.2 ± 5.6	4.1	1
SH04	Pot.	693189	4230179	429	Quartzite	4.58 ± 0.79	51.3 ± 4.2	13.6	0
SH18	Pot.	730112	4282749	380	Metabasalt	4.6 ± 0.39	56.3 ± 5.5	4.1	1
SH26	James	708069	4241013	619	Metabasalt	10.01 ± 0.79	50.6 ± 8.1	2.6	1
SH31	Pot.	692434	4225858	482	Quartzite	7.03 ± 0.57	44.4 ± 3.3	8.5	0
SH37	Pot.	697284	4236291	464	Quartzite	7.74 ± 0.62	49.4 ± 5.6	1.5	1

SH39	Pot.	694143	4232771	512	Quartzite	8.62 ± 0.82	59.5 ± 5.7	3.1	1
SH40	James	702052	4234759	568	Metabasalt	7.47 ± 0.61	63.7 ± 5.8	3.3	0
SH54	Pot.	699080	4240433	496	Quartzite	14.25 ± 1.1	52.4 ± 8.6	1.8	1

^A JSQ samples from Portenga and Bierman (2011). POT samples from Portenga et al. (2019). SH samples from Duxbury et al. (2015).

^B Abbreviations: Susquehanna (Susq.), Potomac (Pot.)

^C UTM Zone 17

^D Denotes whether channel profiles from basin above sample are consistent with topographic equilibrium (1) or whether these display non-equilibrium characteristics (0)

Supplementary References

- Bierman, P., & Steig, E.J. (1996). Estimating rates of denudation using cosmogenic isotope abundances in sediment. *Earth Surface Processes and Landforms*, 21, 125-139.
- Dicken, C.L., Nicholson, S.W., Horton, J.D., Kinney, S. A., Gunther, Gregory, Foose, M. P., & Mueller, J. A. L. (2005). Preliminary integrated geologic map databases for the United States: Delaware, Maryland, New York, Pennsylvania, and Virginia: U.S. Geological Survey Open File Report 2005-1325, accessed January 31, 2013, at <http://pubs.usgs.gov/of/2005/1325/>
- Duxbury, J., Bierman, P. R., Portenga, E. W., Pavich, M. J., Southworth, S., & Freeman, S. P. (2015). Erosion rates in and around Shenandoah National Park, Virginia, determined using analysis of cosmogenic ¹⁰Be. *American Journal of Science*, 315(1), 46-76. <https://doi.org/10.2475/01.2015.02>
- Granger, D.E., Kirchner, J.W., & Finkel, R. (1996). Spatially averaged long-term erosion rates measured from in situ-produced cosmogenic nuclides in alluvial sediment. *Journal of Geology*, 104, 249-257.
- Greene, C. A., Thirumalai, K., Kearney, K. A., Delgado, J. M., Schwanghart, W., Wolfenbarger, N. S., & Blankenship, D. D. (2019). The climate data toolbox for MATLAB. *Geochemistry, Geophysics, Geosystems*, 20(7), 3774-3781. <https://doi.org/10.1029/2019GC008392>
- Harkins, N., Kirby, E., Heimsath, A., Robinson, R., & Reiser, U. (2007). Transient fluvial incision in the headwaters of the Yellow River, northeastern Tibet, China. *Journal of Geophysical Research: Earth Surface*, 112(F3). <https://doi.org/10.1029/2006JF000570>
- Miller, S. R., Sak, P. B., Kirby, E., & Bierman, P. R. (2013). Neogene rejuvenation of central Appalachian topography: Evidence for differential rock uplift from stream profiles and erosion rates. *Earth and Planetary Science Letters*, 369, 1-12. <https://doi.org/10.1016/j.epsl.2013.04.007>
- Moucha, R., & Ruetenik, G. A. (2017). Interplay between dynamic topography and flexure along the US Atlantic passive margin: Insights from landscape evolution modeling. *Global and Planetary Change*, 149, 72-78. <https://doi.org/10.1016/j.gloplacha.2017.01.004>
- Nicholson, S. W. D., Horton, C. L., Labay, J. D., Foose, K. A., Mueller, M. P., & Julia, A. L. (2005). Preliminary integrated geologic map databases for the United States: Kentucky, Ohio, Tennessee, and West Virginia: U.S. Geological Survey Open File Report 2005-1324, accessed January 31, 2013, at <http://pubs.usgs.gov/of/2005/1324>

- Perron, J. T., & Royden, L. (2013). An integral approach to bedrock river profile analysis. *Earth Surface Processes and Landforms*, 38(6), 570-576. <https://doi.org/10.1002/esp.3302>
- Portenga, E. W., & Bierman, P. R. (2011). Understanding Earth's eroding surface with 10 Be. *GSA today*, 21(8), 4-10. <http://doi.org/10.1130/G111A.1>
- Portenga, E. W., Bierman, P. R., Trodick, C. D., Greene, S. E., DeJong, B. D., Rood, D. H., & Pavich, M. J. (2019). Erosion rates and sediment flux within the Potomac River basin quantified over millennial timescales using beryllium isotopes. *GSA Bulletin*, 131(7-8), 1295-1311. <https://doi.org/10.1130/B31840.1>
- Schwanghart, W., & Scherler, D. (2014). TopoToolbox 2—MATLAB-based software for topographic analysis and modeling in Earth surface sciences. *Earth Surface Dynamics*, 2(1), 1-7. <https://doi.org/10.5194/esurf-2-1-2014>
- Schwanghart, W., & Scherler, D. (2017). Bumps in river profiles: uncertainty assessment and smoothing using quantile regression techniques. *Earth Surface Dynamics*, 5, 821-839. <https://doi.org/10.5194/esurf-5-821-2017>
- Thirumalai, K., A. Singh, and R. Ramesh (2011), A MATLAB code to perform weighted linear regression with (correlated or uncorrelated) errors in bivariate data, *Journal of the Geological Society of India*, 77(4), 377-380. <https://doi.org/10.1007/s12594-011-0044-1>
- Trappitsch, R., Boehnke, P., Stephan, T., Telus, M., Savina, M. R., Pardo, O., Davis, A.M., Dauphas, N., Pellin, M.J., & Huss, G. R. (2018). New constraints on the abundance of ^{60}Fe in the early solar system. *The Astrophysical Journal Letters*, 857(2), L15. <http://doi.org/10.3847/2041-8213/aabba9>
- York, D., Evensen, N. M., Martinez, M. L., & De Basabe Delgado, J. (2004). Unified equations for the slope, intercept, and standard errors of the best straight line. *American Journal of Physics*, 72(3), 367-375. <https://doi.org/10.1119/1.1632486>